Investigation and Measurement of Oscillations of the H.E.S.S. Telescopes

Master's Thesis in Physics

Presented by

Christian Kupfer

February 16, 2018

Friedrich-Alexander-Universität Erlangen-Nürnberg

Supervisor: Prof. Dr. Christopher van Eldik
Second referee: Prof. Dr. Stefan Funk

Zusammenfassung

Die optische Abbildungsfunktion des H.E.S.S.-Instruments, die für die korrekte Rekonstruktion einer Quelle nötig ist, wird normalerweise durch Monte-Carlo-Simulationen der Teleskop- und Beobachtungsbedingungen ermittelt. In diesen Simulationen wird eine Pointing-Ungenauigkeit angenommen, welche durch eine Verschiebung der Position jedes Teleskops gemäß einer 2D-Gauß-Funktion mit Breite $\sigma = 15''$ modelliert wird [1]. In dieser Arbeit wird der Beitrag von Schwingungen der Teleskopkameras im Frequenzbereich zwischen 0.5 Hz und 15.625 Hz zu diesen Pointing-Ungenauigkeiten untersucht. Die Konzeption, Fertigung und Kalibration eines Messinstruments wird beschrieben und die Analysemethode für die Daten wird erläutert. Die Ergebnisse von Schwingungsmessungen an den H.E.S.S.-Teleskopen werden präsentiert und mit Daten aus einer Simulation verglichen. Es wird gefolgert, dass Oszillationen im untersuchten Frequenzbereich nur einen sehr kleinen Beitrag zur Pointing-Ungenauigkeit leisten. Außerdem wird gezeigt, dass eine Änderung des beobachteten Zielobjekts in einigen Fällen einen kleinen, aber nachweisbaren Einfluss auf die Kameraposition während des direkt darauffolgenden Runs haben kann.

Abstract

The point-spread function of the H.E.S.S. experiment, which is necessary for a proper source reconstruction, is usually determined by conducting Monte-Carlo simulations of the instrument and observation conditions. As part of these simulations, a pointing uncertainty is introduced by offsetting the position of each telescope during the run by a 2D Gaussian with width $\sigma = 15''$ [1]. In this thesis, the contribution to the pointing uncertainties from telescope camera oscillations with frequencies between 0.5 Hz and 15.625 Hz is investigated. The design, assembly and calibration of a measurement device is described and the analysis methods for the data are presented. The results from oscillation measurements performed at the H.E.S.S. telescopes are displayed and compared with simulated data sets. It is concluded that oscillations in the examined frequency range contribute only a very small fraction to the pointing uncertainties. Additionally, it is shown that in some cases, telescope pointing transitions can have a small but noticeable impact on the camera position during the immediately following observation run.

Contents

1. Introduction

Ever since the discovery of cosmic rays by Victor F. Hess in 1912 [2], astronomers have been trying to uncover the details of their origin. While the lower energetic share of cosmic particles up to 10^{15} eV is believed to be produced by galactic sources, cosmic rays of even higher energies require powerful acceleration mechanisms absent in our home galaxy. The high end of the cosmic ray spectrum is therefore especially interesting for the investigation of extragalactic objects such as active galactic nuclei, supernova remnants or pulsar wind nebulae [3]. These objects are able to accelerate charged particles up to and even beyond energies of 10^{20} eV, vastly exceeding those of any particle accelerator experiment on earth (LHC centre-of-mass energy: $13 \cdot 10^{12}$ eV [4]). As a result, cosmic radiation is not only of interest for astronomy but also in the field of high energy physics.

While cosmic radiation consists of different particles including protons, heavier atomic nuclei and, to a lesser extent, electrons, all of these charged particles get deflected in intergalactic magnetic fields, retaining very little directional information upon reaching earth [5]. For this reason, charged particles are unfit for imaging astronomy or the exact determination of the accelerating source's position. This limitation can be bypassed by looking at gamma rays instead of charged messenger particles. Such high energetic photons get produced when charged primary particles scatter with the cosmic microwave background, magnetic fields or radiation from stars or through collision with molecular clouds or interstellar gas [3]. Due to their uncharged nature, gamma rays can travel straight from their point of origin towards earth, allowing us to gather information about the source responsible for the acceleration. Additionally, the acceleration process itself can be investigated through the energy distribution of the photons which directly represents that of the charged particles in the emergence region [6].

However, the detection of these high energetic gamma rays is hindered by earth's atmosphere which is opaque for photons of these wavelengths. One possible way around this problem is space-based astronomy with telescopes mounted on satellites. However, this puts strong limitations on weight and size of the detector and thus limits the possibility for detections in the high energy range [7].

Another option is the so-called Imaging Atmospheric Cherenkov Technique which uses the air in the atmosphere as a detection medium: an incoming gamma ray produces a shower of secondary particles via a cycle of pair-production and emission of bremsstrahlung in the atmosphere. Because these secondary particles can travel faster than the phase velocity of light in air, Cherenkov radiation is emitted. Since the wavelength of the Cherenkov light is in the visible range, it can traverse the atmosphere freely, allowing for detection with ground-based telescopes [7]. This technique is currently employed by several experiments such as MAGIC, VERITAS and the **H**igh **E**nergy **S**tereoscopic **S**ystem (H.E.S.S.).

This work focuses on measuring oscillations of the H.E.S.S. telescope cameras in an attempt to explain the pointing uncertainties assumed in Monte-Carlo simulations of the point-spread function. Chapter 2 introduces the essentials of gamma-ray astronomy and the H.E.S.S. telescopes. Chapter 3 covers the design of the measurement device, including the initial requirements, the developed hardware and software and the conduct of the actual measurement. The following chapter 4 describes the calibration procedure performed for the sensor and chapter 5 explains the different analysis steps and methods on a set of simulated and real data. In the end, chapter 6 gives a summary of the results so far.

2. Gamma-ray astronomy and the H.E.S.S. experiment

The goal of H.E.S.S. is to improve the understanding of acceleration, propagation and interactions of gamma rays with energies from the GeV to the TeV range. The experiment, located in the Khomas highland roughly 100 km south-west of the Namibian capital Windhoek, consists of five individual Cherenkov telescopes: four small-size telescopes with a mirror dish of 12 m diameter called CT1 through CT4 and a single large telescope with a total mirror area of 614 m^2 called CT5. The initial setup officially started operating in 2004 and was composed of only the four smaller telescopes arranged in a square shape with a side length of 120 m (H.E.S.S. phase I). The larger, fifth telescope was added to the centre of the square in 2012 (H.E.S.S. phase II) to allow for a better coverage of the low energy region as well as improved sensitivity [6] (see Fig.1).

Figure 1: Picture of the H.E.S.S. site showing the large telescope in the centre of the four smaller telescopes.

2.1. Telescope characteristics

The mount of the telescopes consists of the base frame and the dish, both of which are built from steel frames to satisfy the need for high stability and rigidity. The base frame can be rotated by a motor-controlled drive system on circular rails with a diameter of roughly 14 m for the smaller telescopes and 36 m for the large telescope [8][9]. This, in conjunction with the capability of the dish to rotate around the elevation axis, allows pointing to an arbitrary position in the sky. The pointing is governed by angular position encoders, which reach a precision in the order of a few arc-seconds. However, the pointing accuracy is limited not by the encoders but by effects due to bending and distortion of the telescope structure. To correct deviations in the telescope pointing, an optical guidance telescope with a CCD camera is used [10].

The mirrors of the H.E.S.S. telescopes focus the incoming Cherenkov light onto the cameras and are to a large part responsible for the image quality. The small-sized telescopes use mirrors composed of 382 individual circular facets, each with a diameter of 60 cm leading to a total mirror area of 107 m^2. Once mounted onto the support structure, the orientation of each mirror facet can be remotely controlled. A fully automated process aligns the individual tiles by converging the light spots, created by the facets when pointing at a star, on the centre of the lid of the Cherenkov camera [11]. The mirror of the large 28 m telescope consists of 875 hexagonal facets aligned on an approximately parabolic shape for a total mirror area of 614 m^2.

The cameras of the small-sized telescopes consist of 960 pixels each, covering a combined field of view of 5°. Photomultiplier tubes with a gain of $2 \cdot 10^5$ are used to amplify the incoming photon signal [12]. A coincidence unit between multiple pixels controls the trigger system of the camera, leading to good rejection of night sky background photons. Images are saved only if either multiple telescopes trigger simultaneously, providing a stereoscopic view of the events [13], or if the large CT5 telescope triggers. During periods of bad weather, the camera is angled towards the ground and is sheltered inside a hut.

The camera of the large 28 m telescope employs a similar design as its smaller counterpart, however, it contains a total of 2048 pixels and has received several small improvements. Due to the larger focal length of 36 m compared to 15 m with unchanged pixel size, the resolution is greatly improved by roughly a factor of 2.4. In contrast to its predecessor, the camera of the large telescope needs to be demounted during bad weather conditions [14].

2.2. Production and detection of gamma rays

Black body radiation originating from hot matter is the source of a significant fraction of lower energetic cosmic gamma radiation, however, it cannot account for photons in the highest energy range [3]. This so-called thermal radiation is emitted by all objects and the arising energy spectrum is almost solely dependant on the temperature of the object. In terms of frequency, this is described by Planck's law [15]:

$$B_\nu(T) = \frac{2\mathrm{h}\nu^3}{\mathrm{c}^2} \frac{1}{\mathrm{e}^{\frac{\mathrm{h}\nu}{\mathrm{k}T}} - 1} \tag{1}$$

Here, $B_\nu(T)$ is the spectral radiance, h is the Planck constant, ν is the frequency, c is the speed of light, k is the Stefan-Boltzmann constant and T is the temperature of the body. This spectrum assumes its maximum at a wavelength given by Wien's displacement law which scales inversely with the temperature. Thermal radiation is a feasible explanation for gamma rays with energies up to several keV, however, there are no known sources with sufficient temperatures to produce GeV-, or even TeV-photons [3].

Beyond the thermal energy regime, gamma rays are produced by so-called non-thermal accelerators. Contrary to thermal radiation, these sources produce photon fluxes with energy spectra obeying a power law $\frac{\mathrm{d}N}{\mathrm{d}E} \propto E^{-\alpha}$ with a typical value of α between 2 and 3. Objects of this category are believed to primarily accelerate charged particles via electromagnetic interactions which in turn produce high energy gamma rays by interactions with the ambient medium. This can either be collisions with surrounding matter or scattering on radiation fields [16]. Two main production mechanisms - hadronic and leptonic channels - are distinguished for high energy gamma rays [5].

Hadronic interactions between protons or heavier nuclei and the surrounding medium can result in the production of pions amongst other particles. Pions are mesons composed of (anti-)up- and (anti-)down-quarks and come in charged or neutral variations. Charged pions decay almost exclusively into muons and muon-neutrinos (and their respective antiparticles) via the weak interaction. Neutral pions on the other hand, decay by means of the electromagnetic force, with a decay resulting to over 98% in two photons:

$$\pi^0 \rightarrow \gamma + \gamma \tag{2}$$

The leptonic production channel for high energy gammas is governed by the electromagnetic interaction of strongly accelerated electrons with ambient photons of lower energy (e.g. cosmic microwave background, infrared or optical photons). During the scattering process, the electron transfers part of its energy to the photon, resulting in a reduction of the photon wavelength. This 'up-scattering' of a photon to higher energies is called inverse Compton scattering in analogy to the classical Compton effect where the energy transfer is reversed.

$$\mathrm{e}_{\text{high energy}} + \gamma_{\text{low energy}} \rightarrow \mathrm{e}_{\text{low energy}} + \gamma_{\text{high energy}} \tag{3}$$

Electrons can also produce gamma radiation via synchrotron losses in local magnetic fields, however, the energy of these gamma rays is usually smaller than that of photons from inverse Compton scattering [6]. The brightest persistent TeV point source observed by H.E.S.S. is the Crab Nebula, which is usually used as a benchmark.

In order to detect gamma rays, H.E.S.S. makes use of the Imaging Atmospheric Cherenkov Technique [17]: upon entering earth's atmosphere, the high energetic photon interacts, producing an electron-positron pair. Due to conservation of momentum, this process requires the presence of an atomic nucleus. Both secondary particles can then emit photons again during the deceleration in air via bremsstrahlung. These photons usually have enough energy to undergo pair-production themselves, repeating the process until the minimum required energy for pair-production is no longer available and the cascade stops. The charged secondary particles can travel through the atmosphere at speeds exceeding the phase velocity of light in air. This leads to the emission of Cherenkov light by the medium surrounding the travel path of the particle. Because the spectrum of Cherenkov radiation usually peaks at wavelengths in the visible range, a detection of the Cherenkov light by ground-based telescopes is possible, bypassing the limitations of space-based astronomy.

The shower usually reaches its maximum number of particles at roughly 10 km height and begins to fade away closer towards earth. The Cherenkov light is emitted in a cone shape with a typical opening angle of roughly 1°, illuminating an area of over 30000 m^2 on the ground. The telescopes located in this Cherenkov light pool focus the incoming photons onto highly sensitive, segmented photomultipliers. This way, a projected image of the air shower is taken and image processing software can be used to obtain the shower parameters. The direction of the shower in the image points towards the origin of the gamma ray and the image intensity relates to its energy [17]. If multiple telescopes are illuminated, a stereoscopic reconstruction of the shower geometry and thus of the direction and energy of the incident gamma photon is possible.

To produce an image of a celestial object, a large number of gammas need to be detected from that specific source. The quality of the image strongly depends on accurately knowing the observation and instrument conditions which were prevalent during the measurement. This includes the position of the telescope cameras upon the arrival of each shower to precisely reconstruct the incident direction of the gamma-ray [1]. The error of the camera positions specifically caused by oscillations e.g. due to wind will be investigated in the following.

3. Acceleration measurement

There are objects in the sky that are either too small or too far away to be spatially resolved by H.E.S.S.. The apparent size of an observed object results from a combination of its intrinsic size and the imperfect detector response, called **P**oint-**S**pread **F**unction (PSF). Therefore, in order to properly determine the true size of a source, the widening due to the PSF needs to be corrected. The PSF is obtained via Monte-Carlo simulations of the telescope system for different observational parameters. An analysis of more than ten point-like sources [18] revealed intrinsic source sizes for these objects between 0.015° and 0.03°, dependent on the chosen event cuts. Because all these sources, independent of type and distance, show similar extensions that are incompatible with a point-like nature of the object, a systematic underestimation of the PSF is suggested. If the PSF is underestimated, the correction to the apparent source size is too small, leading to seemingly extended point-sources.

A study performed more recently [19] was able to resolve the extension of the Crab nebula, an object which previously appeared point-like when imaged with the H.E.S.S. telescopes. This was done with a more sophisticated, time-dependent simulation of the observation and instrument conditions, yielding a more accurate estimate of the PSF. The results, depicted in Fig.2, show a clear extension of the Crab nebula, while other investigated point-sources retain their point-like nature.

As part of the simulation, pointing uncertainties were modelled by offsetting the position of each telescope according to a 2D Gaussian with width $\sigma = 15''$ [1]. One imaginable effect that could lead to these uncertainties is an oscillation of the telescope camera, resulting in a time-dependent displacement from its nominal position. Such an oscillation may be induced by wind on the telescope site, by small bumps in the rail when the telescope is rotated during tracking, or by residual movement at the start of a run after the target of observation was changed. In order to investigate these possibilities, a measurement with the intention of finding and characterizing possible oscillations is performed.

The measurement is conducted using a self-developed and self-built acceleration sensor. In the following chapters, the sensor requirements and characteristics, hardware components and the software are described.

3.1. Sensor requirements

In order to measure a possible camera oscillation, the sensor needs to be sensitive to both the frequency and the amplitude of the oscillation.

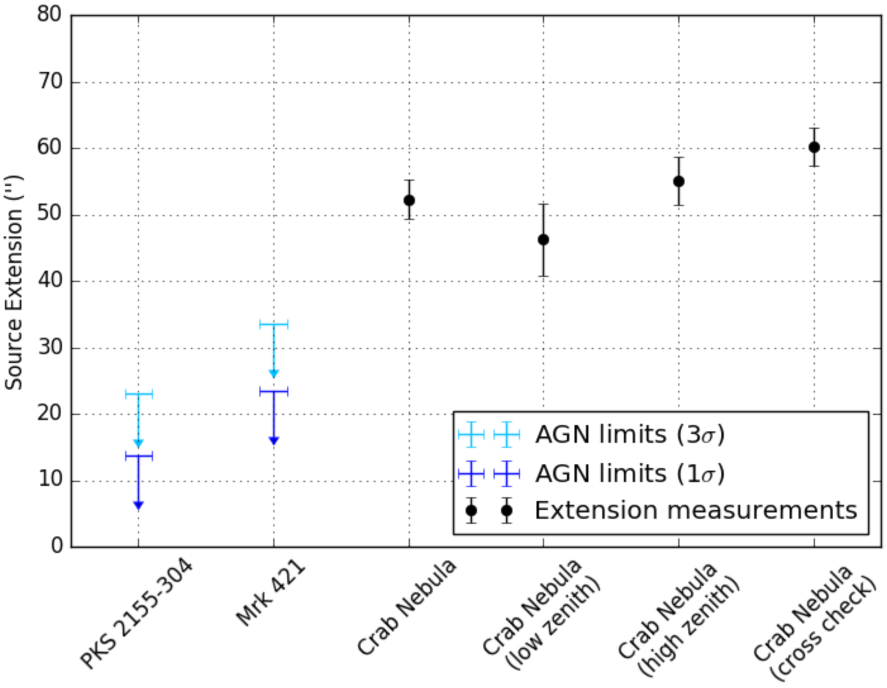

Figure 2: Source extension limits of PKS 2155-304 and Markarian 421 and the observed source extension of the Crab nebula for zenith angles in the range of 44° – 46° (low zenith) and 46° – 55° (high zenith). The cross check was performed with an independent method of calibration, reconstruction and analysis. Figure taken from [19].

For an estimate of the oscillation frequency, the results from a finite element model analysis, conducted for the **M**edium-**S**ized **T**elescopes (MST) of the planned **C**herenkov **T**elescope **A**rray (CTA), were examined [20]. Even though the MST differs significantly in terms of design, it can still be used as a reference for a rough estimation of the mechanical properties of the small H.E.S.S. telescopes. The MST model analysis reveals the lowest eigenfrequency at slightly above 1.5 Hz, with the first ten eigenfrequencies below 6 Hz (see table 1). Assuming a sufficient similarity between the medium-sized CTA telescopes and the small H.E.S.S. telescopes, it is reasonable to expect eigenfrequencies of the same order.

The amplitude of the oscillation can be estimated from the width of the Gaussian σ which was used to model the camera displacement in the study of the Crab nebula extension [19] .

From these two estimates, the resulting acceleration occurring at the camera body can be calculated. For a simple sinusoidal oscillation of the form

Mode	Frequency [Hz]
1.	1.5478
2.	2.0501
3.	2.7603
4.	3.6644
5.	3.8607
6.	3.9135
7.	4.0912
8.	4.4064
9.	5.4372
10.	5.7906

Table 1: First ten eigenfrequencies found in a simulation for the medium sized CTA telescopes. Taken from [20].

$$d(t) = A \cdot \sin(\omega \cdot t) \tag{4}$$

with amplitude A and radial frequency ω, the acceleration $a(t)$ is given by the second derivative w.r.t. time:

$$a(t) = \ddot{d}(t) = -A \cdot \omega^2 \sin(\omega \cdot t) \tag{5}$$

Furthermore, with the substitution $x = \omega t$, the root-mean-square (RMS) displacement d_{RMS} of the oscillation can be derived [21]:

$$\begin{aligned}
d_{\mathrm{RMS}} = & \sqrt{\frac{1}{2\pi}\int_0^{2\pi} d^2(x)\,\mathrm{d}x} && (6)\\
= A \cdot & \sqrt{\frac{1}{2\pi}\int_0^{2\pi} \sin^2(x)\,\mathrm{d}x} && (7)\\
= A \cdot & \sqrt{\frac{1}{2\pi}\int_0^{2\pi} \frac{1}{2}\left(1-\cos(2x)\right)\,\mathrm{d}x} && (8)\\
= A \cdot & \sqrt{\frac{1}{2} - \int_0^{2\pi} \cos(2x)\,\mathrm{d}x} && (9)\\
= & \frac{A}{\sqrt{2}} && (10)
\end{aligned}$$

For the RMS displacement of the oscillation to be equivalent to the Gaussian that was used to model the pointing uncertainties with width $\sigma = 15''$, the condition $d_{\mathrm{RMS}} = D \cdot \tan(\sigma)$ needs to be fulfilled. Here, D is the focal length of the telescope.

Therefore, the oscillation amplitude is given by $A = \sqrt{2} \cdot D \cdot \tan(\sigma)$. The radial frequency ω is calculated from the oscillation frequency ν as $\omega = 2\pi\nu$. Therefore, the resulting acceleration is given by:

$$a(t) = -4\pi^2\nu^2 \sqrt{2}\, D \, \tan(\sigma) \cdot \sin(2\pi\nu \cdot t) \tag{11}$$

The maximum acceleration is then given by $a_{\mathrm{max.}} = 4\pi^2\nu^2 \sqrt{2}\, D \, \tan(\sigma)$. Inserting explicit values in accordance with the previously provided arguments yields a value of $a_{\mathrm{max.}} = 0.061$ m/s^2 with parameters $\nu = 1$ Hz, $D = 15$ m and $\sigma = 15''$. This can be expressed in terms of gravitational acceleration ($g = 9.81$ m/s^2) as:

$$a_{\mathrm{max.}} = 6.2 \ \cdot 10^{-3}\mathrm{g} \tag{12}$$

The camera displacement, given by eq.(4), reaches a maximum value of:

$$d_{\mathrm{max.}} = A = \sqrt{2} \cdot D \cdot \tan\sigma = 1.543 \text{ mm} \tag{13}$$

and the RMS displacement of this oscillation is given by:

$$d_{\mathrm{RMS}} = \frac{A}{\sqrt{2}} = D \cdot \tan\sigma = 1.090 \text{ mm} \tag{14}$$

Factoring in the several uncertainties in the derivation of this value, the minimum required resolution to obtain significant measurement results is estimated to $1.5 \cdot 10^{-3}$ g. This result is used as a baseline for the selection of a measuring device.

3.2. Hardware

Beyond the resolution and frequency requirements previously discussed, several other key features are mandatory to perform a successful measurement:

- A way to store acceleration data internally or transmit it to a remote computer for later analysis

- An internal power supply for wireless operation
- The ability to provide absolute date- and timestamps for the measurement points to correlate them with relevant data from other sources

This chapter gives an overview over the components used to build the measurement device and highlights some of their key features and characteristics.

3.2.1. Accelerometer

The actual acceleration measurement is performed by a commercial evaluation board for the ADXL355 accelerometer manufactured by *Analog Devices* [22]. It is a so-called **M**icro **E**lectro **M**echanical **S**ystem accelerometer that senses the acceleration by measuring the change in capacitance between a seismic mass and two electrodes. The seismic mass is suspended in between the two electrodes with a small gap, effectively forming a plate capacitor on each side. When the device is accelerated, the seismic mass moves and the capacitance of either capacitor changes. This change is measured and translated to an acceleration value [23]. A schematic of such a capacitive MEMS accelerometer is depicted in Fig.3.

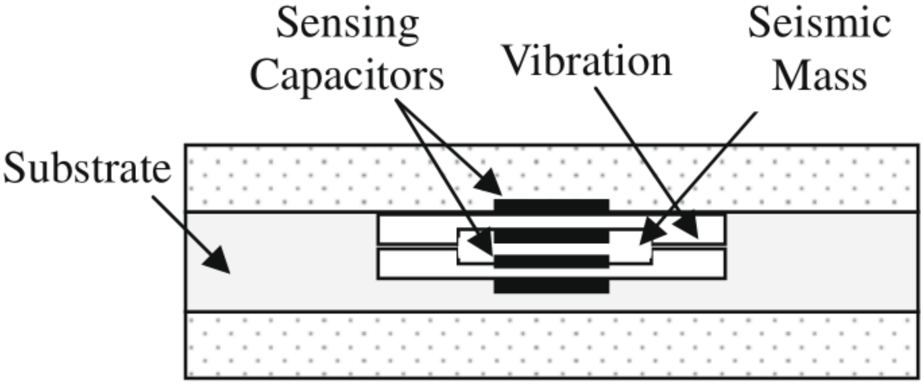

Figure 3: Schematic of a capacitive accelerometer. The seismic mass suspended between two electrodes forms a plate capacitor on either side. The change in capacitance from a force acting on the mass can be translated to an acceleration value. Figure taken from [23].

The ADXL355 provides three perpendicular measurement axes with low noise density of $\rho_n = 25 \ \cdot 10^{-6}\mathrm{g}/\sqrt{\mathrm{Hz}}$ and a frequency response between the DC level and a selectable threshold up to 1 kHz. The noise density of the accelerometer describes the amount of noise in a given frequency band. The intrinsic accelerometer noise is composed of electronic noise from the circuitry and mechanical noise from vibrations of the movable part of the device [24]. The total RMS noise Δa on an otherwise clean signal can be obtained via:

$$\Delta a = \rho_n \cdot \sqrt{(1.6 \cdot B)} \tag{15}$$

where B is the bandwidth chosen for the application. The bandwidth is limited by a combination of a fixed analog low-pass filter with a cutoff frequency of 1.5 kHz and a programmable digital decimation filter [22]. Since the filter doesn't sharply remove all frequencies above the chosen threshold but has a transition region, some of the higher frequency noise remains. To account for this, the factor 1.6 is introduced in eq.(15) according to the information given by the manufacturer [25]. For the chosen filter setting, the ADXL355 provides data sampled at a frequency of $f_S = 62.5$ Hz.

Since the frequencies targeted in this study were estimated to be in the lower Hertz regime, the filter setting with a cutoff frequency of 15.625 Hz is chosen. According to eq.(15), the theoretically expected noise of the sensor in the frequency range between 0 Hz and 15.625 Hz is $125.0 \cdot 10^{-6}$g. Because this value is significantly below the resolution requirement of $1.5 \cdot 10^{-3}$g, the sensitivity of the device is sufficient to detect the suspected oscillations.

The ADXL355 provides an integrated analog to digital converter allowing for direct communication with a processing unit via the SPI protocol (see chapter 3.3). It is also equipped with a so-called FIFO (**F**irst **I**n **F**irst **O**ut) register that allows data to be stored for a short amount of time before it is read (see chapter 3.3 for more details).

3.2.2. Microcontroller

The microcontroller board responsible for the communication and coordination of the peripheral devices is an Arduino UNO Rev. 3 [26]. It is an open-platform circuit board that features a microcontroller, several programmable digital input/output pins as well as analog connectors. It can be powered through a USB-B plug or via power jack with a supply voltage of 7 V to 12 V and can be programmed via USB port through the Arduino development environment. The programming language is based on the C/C++ language with a set of special functions.

3.2.3. GPS and data storage

The core functionality of the Arduino UNO can easily be extended via so-called shields, i.e. piggy-back boards, which can be plugged directly onto the microcontroller board.

This enables customization of the Arduino's capabilities and thus allows it to adapt to different tasks. In this setup, the Adafruit Ultimate GPS Logger Shield is used to provide both the ability to receive GPS data as well as store acceleration data onto a micro-SD card [27]. It is equipped with a small on-board GPS receiver, which can be extended with an external antenna and a 12 mm coin cell to keep track of the time even when the device is turned off. This enables the storage of timing data even in the case that no GPS signal can be received after the device is turned on.

3.2.4. Further components

Logic-Level converter: The Arduino UNO operates on digital logic levels between 0 V(LOW) and 5 V(HIGH) while the ADXL355 uses 3 V as its logic HIGH. Because of this difference, the voltage levels need to be adjusted in order to prevent damage to the accelerometer and enable proper communication. This is done via a bi-directional Logic-Level converter.

Power Source: In order to provide power to the microcontroller without the need for a power connection, a powerbank with a capacity of 10000 mAh is used. It can be charged via USB cable and provides 5 V of power through a USB output that can be connected to the microcontroller's USB port.

3.2.5. Assembly and Housing

For the assembly, the pin headers of the GPS Logger shield and the ADXL355 were soldered into their destined locations. The Logic-Level converter was soldered onto the free area of the shield and connected to the appropriate pins. The GPS Logger shield was then attached to the Arduino UNO without the need for additional wiring by plugging the previously installed pins into the female pin headers of the Arduino UNO. The ADXL355 was connected to the Logic-Level converter and the Arduino UNO according to the data sheet of the device (see appendix A for wiring diagram). Additionally, a status LED was attached to one of the remaining programmable outputs of the microcontroller and a switch was installed between the powerbank and the Arduino UNO to be able to cut the power and turn the sensor off.

All components were built into a plastic housing to provide protection against dust and spray water and allow for easier mounting. In order to minimize dampening effects, the connection between the ADXL355 and the housing of the device has to be very rigid. To achieve this, the accelerometer was screwed onto an acrylic glass plate. The plate was threaded and suspended inside the housing via screws. In addition to the threading, nuts were used to keep the acrylic glass plate in place (see Fig.4). The microcontroller with the GPS module on top was also fixed to the plate. The status LED and switch were broken out of the housing to provide access from the outside. Additionally, a USB cable connected to the power source was driven out of the case to allow charging without opening the housing. These break-out connections were re-sealed using hot glue.

3.3. Software

The communication between the microcontroller and the peripheral devices is handled via **S**erial **P**eripheral **I**nterface (SPI) which makes use of the master/slave principle. It employs a single master device which controls one or multiple slave devices. In this particular case the Arduino UNO acts as the master device while both the GPS shield and the ADXL355 are connected as slave devices. The communication is handled via four channels (see also Fig.5):

The **S**erial **C**loc**K** is used to synchronise the transmission of data between all devices. It is provided by the master device and shared between all slaves.

The **M**aster **O**ut **S**lave **I**n is used for the directional data transfer from the master to all slave devices.

The **M**aster **I**n **S**lave **O**ut is used to transfer data from all the slave devices to the master device.

Additionally, there is one **S**lave **S**elect line for each device, which is used to enable or disable the communication with the specific peripheral. This way, the master can choose which slave device(s) to send data to and receive data from, even though the communication lines are shared between all of them. In order to receive data from a slave device, the master device has to send a `read` command to that specific device first. This prevents the different peripherals from sending data at the same time, which would lead to parts of the data being corrupted.

For the GPS Logger Shield open-source libraries for accessing both the SD card and the GPS receiver are available from the Adafruit website [27]. These can simple be included in the main program of the Arduino UNO to access their functionality.

Since there was no available library for the communication with the ADXL355, an own implementation was written. In order to change the measurement settings the, internal registers of the accelerometer have to be accessed. For this, at least basic `read` and `write` commands are necessary. To ensure the readability of the main program and to avoid errors while programming, special commands for the most used operations were developed. This includes reading out and changing the measurement range and the filter

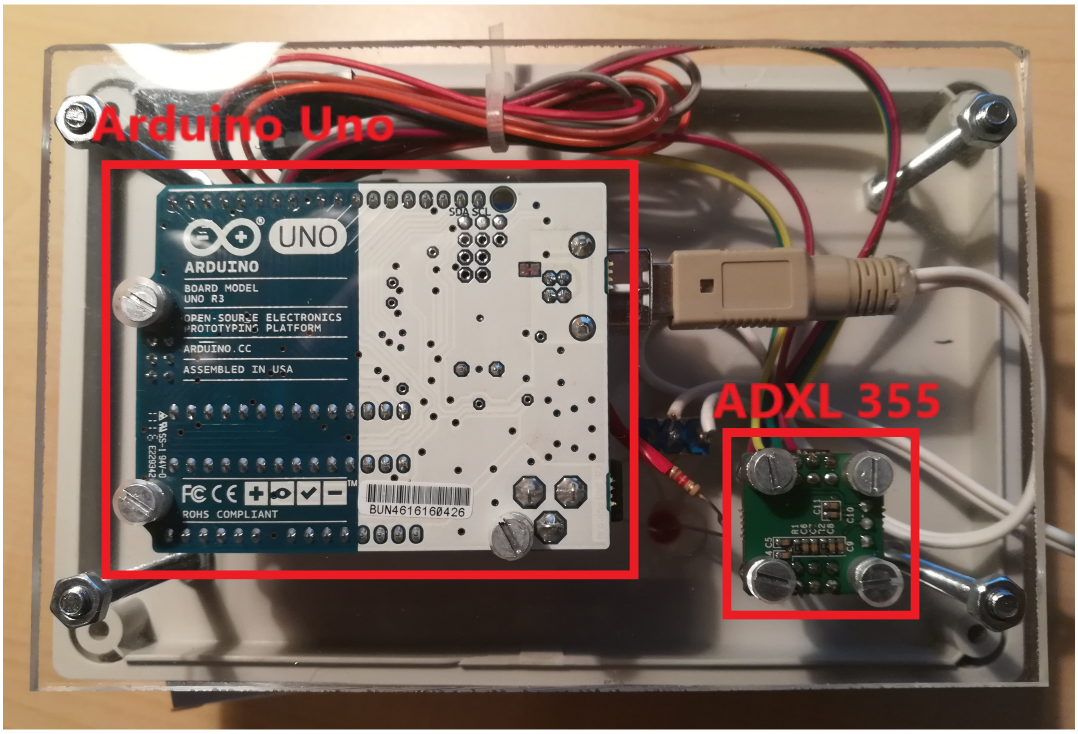

(a) Bottom view: Showing the accelerometer and the microcontroller with the USB power plug, screwed to the acrylic glass plate

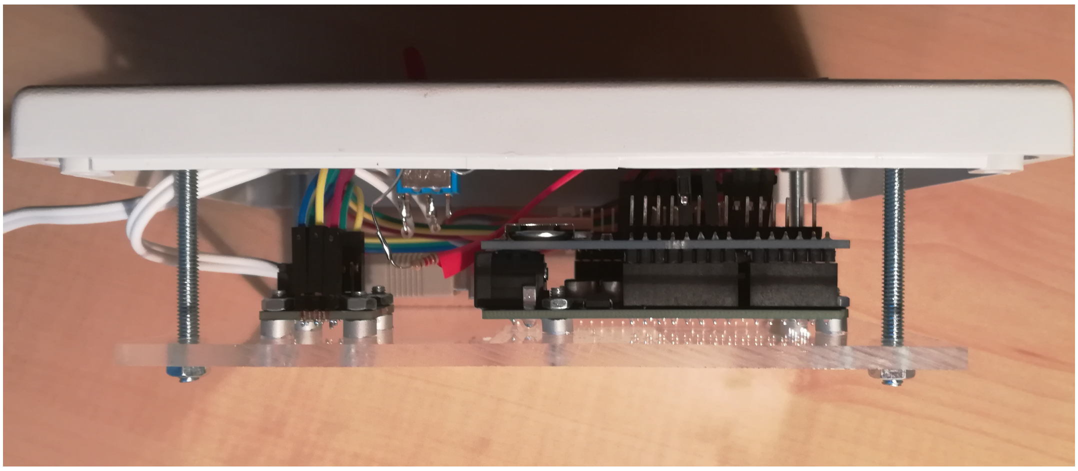

(b) Side view: Showing the GPS logger shield stacked on top of the Arduino and the suspension screws holding the plate in place

Figure 4: Pictures of the accelerometer and microcontroller mounted on the acrylic glass plate held in place by suspension screws.

cutoff frequency as well as switching between standby and measurement mode. These functions can be accessed via the *ADXL355* class. For a list of the most important commands refer to table 2.

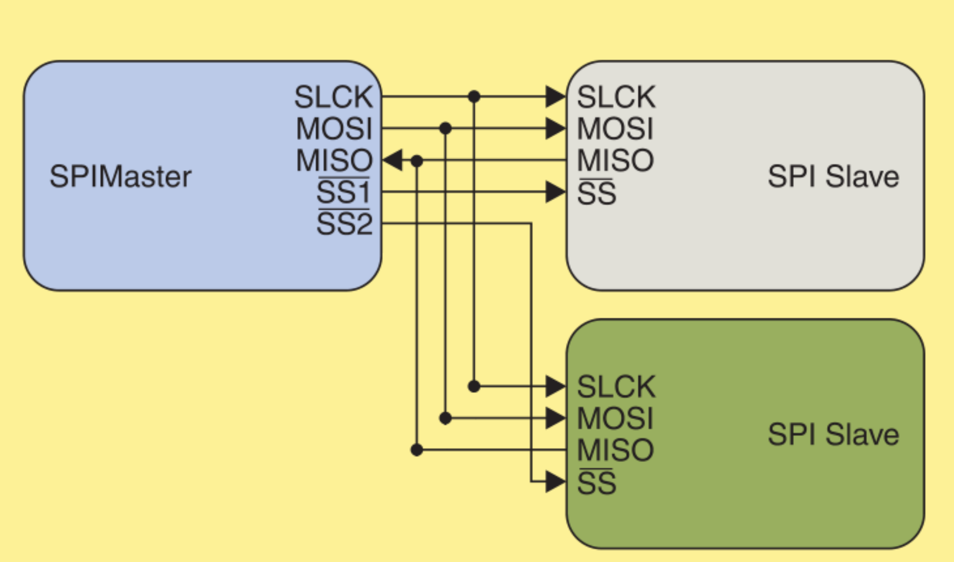

Figure 5: Schematic of the SPI communication between the master device and two slave devices. Figure adapted from [28].

Command	Description
ADXL355	Constructor for the ADXL355 class, required for the other commands
enterStandby	Enter the standby mode, required to change most settings
setFilter	Set the cutoff frequency of the internal low-pass filter
setRange	Set the measurement range in units of g
powerOn	Enter the measurement mode
readAccel	Read the latest acceleration data from all three axis
getTemp	Read the latest temperature data in $°C$
getFIFOSamples	Read the number of samples currently stored in the FIFO
readFIFO	Read the acceleration data from the FIFO, starting with the oldest set

Table 2: Description of the most important commands of the *ADXL355* class.

To read acceleration data from the sensor, one of two methods can be used. The data can be read repeatedly from the registers corresponding to the x-, y- and z-axis, however, since the acceleration data is 20 bits long while each register only contains 8 bits (1 byte) three registers have to be read to access the measurement for each axis. This poses a problem when new acceleration data arrives while the previous data is read out. In this case, it is possible that the three bytes comprising a data point originate from different measurements at different points in time. This mixing of data is undesirable since it can invalidate the measurement results. Furthermore, if the data registers are not read before the next measurement is available, the previous values will be overwritten. This can lead to missing data points if the device can't read the data fast enough e.g. because it is busy storing data on the SD card.

However, the ADXL355 features a so-called FIFO (**F**irst **I**n **F**irst **O**ut), a set of registers that can store up to 96 data sets. Data is read from the FIFO in sets of three data bytes which are guaranteed to correspond to the same measurement and thus the same point in time. When the FIFO is read out, the oldest available data since it was last read is returned first. Because of these properties much less emphasis needs to be put on the correct timing of the readout to guarantee the validity of the data and avoid data loss.

Acceleration data is received in the so-called two's complement notation which is used to represent signed integers as binary numbers [29]. To convert a N-bit binary integer $a = a_{N-1}a_{N-2}...a_0$ from the two's complement representation to a decimal number, the following formula can be used:

$$a = -a_{N-1}2^{N-1} + \sum_{i=0}^{N-2} a_i 2^i \tag{16}$$

This conversion is done by the microcontroller and the values are stored in decimal format on the SD card. Therefore, the acceleration values in units of g can be obtained by multiplying the stored values with the gain of the sensor (see chapter 4.2).

The ADXL355 also includes a temperature sensor that can be utilized to measure the temperature change over the course of the measurement if required. Additionally, the internal clock of the microcontroller can be used to provide relative timestamps.

3.4. Measurement conduct

The completed sensor was taken to the H.E.S.S. site for the shift period from September 8, 2017 to October 10, 2017. There it was fixed to each of the five telescope cameras for a full night of observation. While it was initially planned to attach the measurement box to the backplate of the camera housing via double-sided 'power strips', this was deemed too dangerous to the mirrors in case the box came loose during the operation of the telescope. Therefore, the device was instead placed inside of the camera housing and attached to the bars of the cabinet containing the camera electronics via zipties (see Fig.6(a)). Being inside the metal camera housing prevents the sensor from receiving GPS data, however, timing information can still be retrieved even during offline periods due to the coin cell allowing the GPS module to keep the time even when the device is turned off.

The axes of the accelerometer were aligned in such a way, that the positive z-axis points alongside the optical axis of the telescope, from the camera towards the mirror. The y-axis points towards the bottom of the camera and straight downwards if the telescope is angled at 0° altitude. The x-axis is orientated horizontally and parallel to the altitude rotation axis. The three axes of the sensor employ a left-handed coordinate system.

An exception to this mounting technique was made for the measurement on the large CT5 telescope. Here, the device was attached to a steel beam on the outside of the camera housing as opposed to the inside (see Fig.6(b)). Additionally, the orientation of the device was flipped, causing the y-axis to point upwards at 0° altitude angle and the direction of the x-axis to be inverted compared to the previous case while keeping the z-direction the same relative to the telescope.

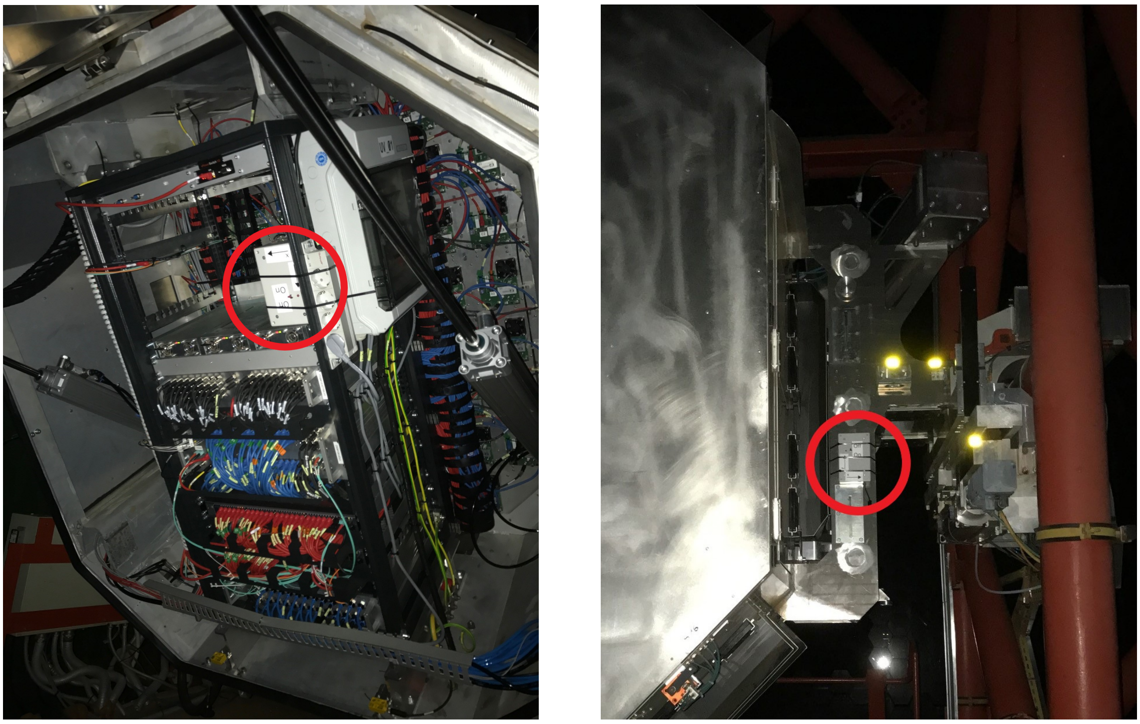

(a) Sensor mounted inside the CT1 camera (b) Sensor mounted on the CT5 camera

Figure 6: Pictures of the measurement device mounted on the telescopes at the H.E.S.S. site in Namibia. While the sensor was mounted inside the camera housing for CT1-4 (a) it was attached outside the camera for CT5 (b).

3.5. Influence of gravity on the measurement

Because the ADXL355 has a frequency response down to the DC level, it can measure constant accelerating forces such as gravity. Therefore, knowing the angle between a specific measurement axis and the direction of the gravitational force is important in order to understand the measured data since any measurement not performed during free fall will be influenced by gravity. This leads to an offset in the measurement along each axis depending on the angle between that axis and the direction of the gravitational force. In case of the idealized alignment described above, this angle depends only on the altitude angle of the telescope for the y- and z-direction, while the x-axis is always perpendicular to gravity and thus uninfluenced by it. From geometrical arguments the amount of acceleration measured due to gravity g for a given altitude angle α can be determined using:

$$g_x = 0 \tag{17}$$

$$g_y = g \cdot \cos\alpha \tag{18}$$

$$g_z = g \cdot \sin\alpha \tag{19}$$

In reality, there is a misalignment compared to the ideal case, caused by several individual alignment errors ranging from the orientation of the sensor chip on the board to the alignment of the box inside the camera housing. This in principle results in small corrections to equations 17 through 19, however, these effects are minor and thus the simple form is sufficient.

4. Sensor calibration

In order to properly interpret the results of the measurement, the sensor has to be calibrated and its characteristics have to be known. The results from this calibration are later included in the analysis of the actual measurement data.

The two main properties of the accelerometer for which a calibration was performed are the gain and the so-called zero-g offset. The calibration procedure for both of these properties is described in the following sections.

4.1. Calibration of zero-g offset

The term zero-g offset describes the acceleration that a sensor measures during a free fall. For an ideal accelerometer this value is zero, however, in reality a non-zero value can result e.g. from limited precision during fabrication.

To determine the zero-g offset, two measurements are performed for each sensor axis. For this, the axis of interest is aligned along the direction of gravity and the acceleration is measured over a period of roughly 20 min. This was done in a room with as little sources of external vibration as possible and the alignment was performed using a level. After the measurement is completed, the box is rotated by 180° such that the axis of interest now points in the opposite direction, then the measurement is repeated. Afterwards, the data points from the start and end of the measurements are truncated to avoid effects from switching the device on or off. The remaining data is a mostly flat line superimposed by the noise from the sensor and possibly residual vibrations that could not be fully avoided. Additionally, some of the measurements performed show a slight gradient which is a result of imperfect attachment to the test surface and a small consequent rotation over time caused by gravity.

To obtain the level of acceleration, a constant fit ($a(t) = a^{\pm} = \text{const.}$) to this dataset is performed yielding values a^+ and a^- for parallel and anti-parallel alignment respectively (see Fig.7). The fit values can be written as the sum of the zero-g offset and the true acceleration $a^{\pm} = a_{\text{Offset}} + a^{\pm}_{\text{True}}$. By demanding an equal value for gravitational acceleration only differing by the sign for both measurements ($a^-_{\text{True}} = -a^+_{\text{True}}$), the offset can be obtained:

$$a_{\text{Offset}} = \frac{a^+ + a^-}{2} \tag{20}$$

Ideally, the two other axes should produce a constant fit at zero acceleration, however, this is not entirely accurate since (1) they are subjected to an offset themselves and (2) the precision of the alignment is limited.

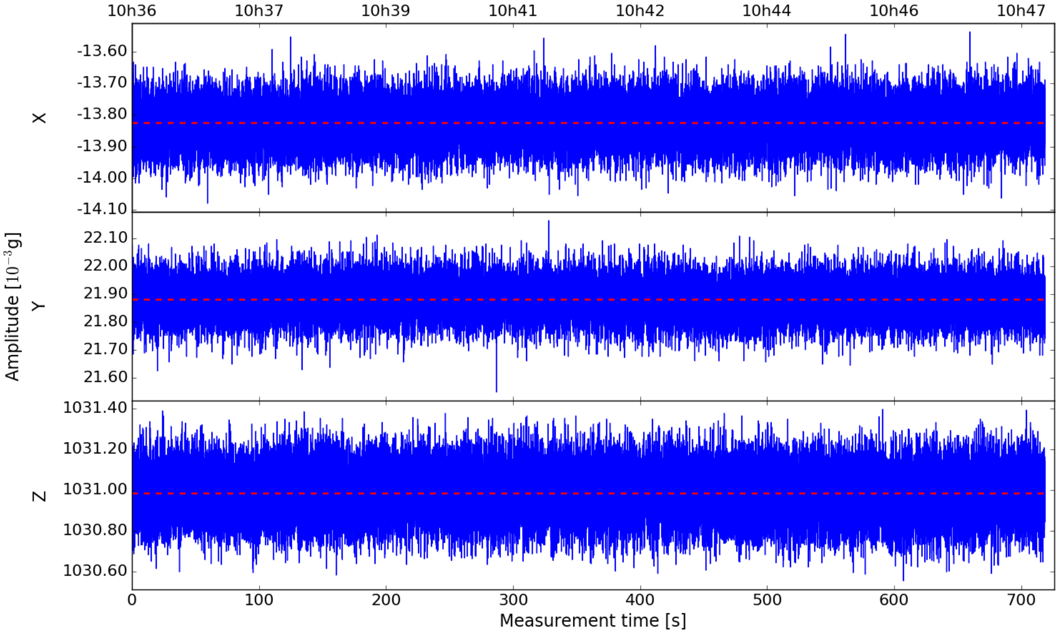

Figure 7: Calibration measurement in positive z-direction with constant fits to the acceleration levels.

The distribution of the acceleration values around the fitted mean are depicted in Fig.8 for all three axes, respectively accompanied by a gaussian fit. It can be seen that the distributions closely follow a normal distribution in each axis, with width $\sigma_{\mathrm{x}} = 6.24 \cdot 10^{-5}$g in the x-direction, $\sigma_{\mathrm{y}} = 6.22 \cdot 10^{-5}$g for the y-direction and $\sigma_{\mathrm{x}} = 1.22 \cdot 10^{-4}$g in the z-direction. The larger value obtained for the z-axis is explained in chapter 4.3. The gaussian behaviour is expected since the noise of the sensor is gaussian as stated in the datasheet [22].

From the width $\sigma_{\mathrm{x,y,z}}$ of the respective distribution and the number of measurement points in the data set N, the error $\Delta a_{\mathrm{x,y,z}}$ of the previously fitted mean value can be calculated. It is given by:

$$\Delta a_{\mathrm{x,y,z}} = \frac{\sigma_{\mathrm{x,y,z}}}{\sqrt{N}} \tag{21}$$

For all conducted calibration measurements it holds that $\Delta a_{\mathrm{x,y,z}} < 2 \cdot 10^{-6}$g. Since this is small compared to other sources of errors such as the limited alignment accuracy, the error from the constant fit is not considered in the following. The acceleration levels for each of the axes obtained from the fit are given in table 3 for each alignment orientation respectively.

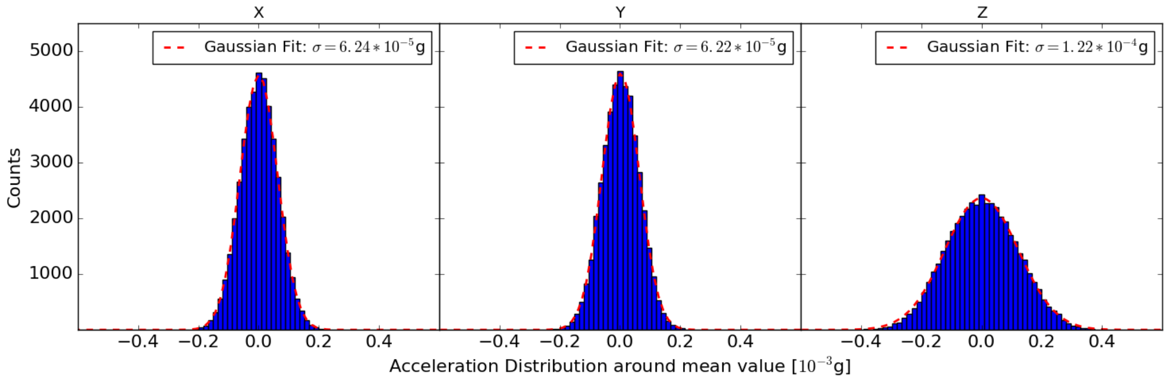

Figure 8: Distribution of acceleration values around the mean value in a calibration measurement where the z-axis was aligned with the direction of gravity. The red dashed lines show gaussian fits to the distributions in each axis.

Fit value: Orientation:	x-axis $[10^{-3}$g]	y-axis $[10^{-3}$g]	z-axis $[10^{-3}$g]
+X	1021.3	19.3	−34.0
-X	−1057.3	5.3	−13.16
+Y	−25.3	1059.1	−31.4
-Y	−11.4	−1031.2	−21.0
+Z	−13.8	21.9	1031.0
-Z	−29.7	−3.8	−1080.2

Table 3: Acceleration values from a constant fit to the calibration measurements for different orientations. Orientation +X/+Y/+Z denotes the measurement where the x/y/z-axis was pointed downwards, parallel to gravity, whereas orientation -X/-Y/-Z is used for the anti-parallel case.

The calculated offsets listed in table 4 are consistent with the typical values of $\pm 25 \cdot 10^{-3}$g mentioned in the datasheet. The errors of the offset values due to misalignment can be estimated by considering the angle α between an axis and the direction of gravity. The angle α is given by:

$$\alpha_{\mathrm{x,y,z}} = \arccos\left(\frac{g_{\mathrm{x,y,z}}}{g}\right) \tag{22}$$

Here, $g_{\mathrm{x,y,z}}$ denotes the acceleration measured in the respective axis and $g = \sqrt{g_{\mathrm{x}}^2 + g_{\mathrm{y}}^2 + g_{\mathrm{z}}^2}$ is the total acceleration. The largest misalignment angle found this way is $\alpha = 2.2°$.

Furthermore, the errors $\Delta a^{\pm}$ of the fit values $a^{\pm}$ compared to perfect alignment can be estimated as:

$$\Delta a^{\pm} = g \mp a^{\pm} \tag{23}$$

A misalignment of the axis of interest during the measurement can only ever decrease the magnitude of the measured acceleration value, therefore it is a systematic error. Because the offset is calculated from two measurements where the systematic errors have opposite signs, the largest possible offset error Δa_{Offset} is given by:

$$\Delta a_{\text{Offset}} = \frac{\max(\Delta a^{+},\, \Delta a^{-})}{2} \tag{24}$$

The offsets and the corresponding errors due to misalignment are shown in table 4.

Axis	Offset $[10^{-3}\text{g}]$
x	-18.0 ± 0.4
y	14.0 ± 0.4
z	-24.6 ± 0.3

Table 4: Zero-g offset obtained from fits to the calibration measurement data along with error estimates due to misalignment.

Another possible error source is the aforementioned gradient over the course of the measurement. To estimate the error resulting from such an effect, the difference in acceleration level at the beginning and end of the calibration measurement is considered. By using this value as an error $\Delta a^{\pm}_{\text{Grad.}}$ of the mean acceleration, the offset error can be obtained via:

$$\Delta a_{\text{Offset, Grad.}} = \sqrt{\left(\frac{\Delta a^{+}_{\text{Grad.}}}{2}\right)^2 + \left(\frac{\Delta a^{-}_{\text{Grad.}}}{2}\right)^2} \tag{25}$$

The value of $\Delta a_{\text{Offset, Grad.}}$ is below $3 \cdot 10^{-5}$g for each of the three calculated offsets, which is significantly lower than the error due to misalignment and can thus be neglected.

4.2. Gain and proportionality factor calibration

The other important property that needs to be calibrated is the gain. It is the inverse of the proportionality factor which describes the ratio between the digital output in bits and the acceleration acting on the sensor. The gain is required to convert the output of the accelerometer from an integer number of bits into an acceleration value in units of g and has a nominal value of $3.9 \cdot 10^{-6}$g/bit as stated in the datasheet.

Since gravity is the only force acting on the sensor during the previously performed calibration measurements, the total acceleration should be exactly 1 g, independent of the orientation of the device. The total acceleration is given by the absolute value of the acceleration vector:

$$a = |\vec{a}| = \sqrt{\sum_{i=1}^{3} a_i^2} = \sqrt{\sum_{i=1}^{3} (a_i^* \cdot s_i)^2} \tag{26}$$

Here, the a_i denote the real acceleration values present during measurement, a_i^* denote the acceleration obtained by assuming the nominal gain from the datasheet and s_i denote correction factors to the nominal gain. By demanding that the total acceleration as given in eq.(26) equals 1 g for all six calibration measurements simultaneously, the s_i can be obtained. This is done by numerically minimizing the function:

$$f(s_1, s_2, s_3) = \left(\sum_{n=1}^{N_{\text{meas.}}} (a_n - 1\text{ g}) \right)^2 = \left(\sum_{n=1}^{N_{\text{meas.}}} \left(\sqrt{\sum_{i=1}^{3} \left(a_{i,n}^* \cdot s_i \right)^2} - 1\text{ g} \right) \right)^2 \tag{27}$$

Here, the $a_{i,n}^*$ are the measurement values from the n-th calibration measurement after the removal of the previously determined zero-g offset and $N_{\text{meas.}} = 6$ is the total number of measurements.

This leads to correction factors which are shown in table 5 alongside the resulting gain and proportionality factor. Additionally, the errors of the correction factors, as produced by the minimization algorithm, are displayed. Errors for the gain and proportionality factor are obtained via error propagation.

The resulting proportionality factors lie within the expected range from 235520 LSB/g to 276480 LSB/g according to the accelerometer specifications from the datasheet [22].

Axis	Correction factor	Gain [10^{-6}g/LSB]	Proportionality factor [LSB/g]
x	0.9621 ± 0.0005	3.752 ± 0.002	266510 ± 140
y	0.9568 ± 0.0005	3.731 ± 0.002	267990 ± 140
z	0.9472 ± 0.0005	3.694 ± 0.002	270690 ± 150

Table 5: Correction factors, gain and proportionality factor resulting from calibration for the three measurement axes. Errors of the correction factors obtained from the minimization algorithm.

4.3. Noise level determination

Besides the calibration of zero-g offset and gain, the measurements performed in a controlled environment can also be used to determine the noise level of the measurement device. By taking data without the sensor being subject to any acceleration varying over time, the noise level is simply given by the standard deviation of the measured data points. To avoid any influence of the aforementioned slight gradient, a linear fit to the measured values was subtracted from the data. For the six measurements taken as part of the calibrations, the standard deviations are given in table 6. The last measurement shows a significantly larger standard deviation in the x- and y-axis, which can most likely be attributed to the influence of external noise since the noise level of the sensor is highly unlikely to change between two subsequent measurements. Therefore, measurement 6 is excluded from the calculation of the average.

Measurement	x-axis	y-axis	z-axis
1	0.0583	0.0582	0.1215
2	0.0584	0.0583	0.1236
3	0.0588	0.0575	0.1211
4	0.0596	0.0583	0.1288
5	0.0599	0.0590	0.1113
(6)	(0.0747)	(0.0682)	(0.1176)
Average	0.0590	0.0583	0.1213

Table 6: Standard deviation of data points in units of 10^{-3}g for each axis during the six calibration measurements. Measurement number 6 not included in the average due to differences in the standard deviations that can likely be attributed to external noise.

Comparing the remaining values to the theoretical noise level of $0.125 \cdot 10^{-3}$g obtained from eq.(15) shows that the noise for x- and y-axis is about a factor of 2 smaller than the predicted value. On the other hand, the measured standard deviations for the z-axis agree reasonably well with the theoretical expectation. The difference between the x- and y-direction and the z-axis is likely attributed to the difference in orientation on the chip. While both x- and y-axis lie plain on the chip, the z-direction is perpendicular to it, possibly explaining this peculiar behaviour.

It can be concluded that the actual noise level of the sensor is compatible with the predicted values along the z-axis and even lower for measurements in the other two directions. Therefore, the theoretical noise level can be used to give an estimate of the resolution of the device. Assuming a sinusoidal oscillation with amplitude A and angular frequency ω yields an acceleration amplitude of $a_{\text{max.}} = A \cdot \omega^2$ (compare eq.(5)). Since the signal can not be detected if this value is below the noise level, the resolution limit for such oscillations is given by $A \cdot \omega^2 = 0.125 \ \cdot 10^{-3}$g. Fig.9 shows the limiting resolution for the oscillation amplitude as a function of frequency $\nu = \frac{\omega}{2\pi}$. It can be seen that for purely sinusoidal oscillations with very small frequencies, a large amplitude is required for detection, e.g. an oscillation at a frequency of 0.05 Hz is only detectable with an amplitude of over 12.4 mm, whereas for a 2 Hz oscillation an amplitude of 7.8 µm would suffice. This can be further improved by applying proper filtering to the data (see chapter 5.2.3).

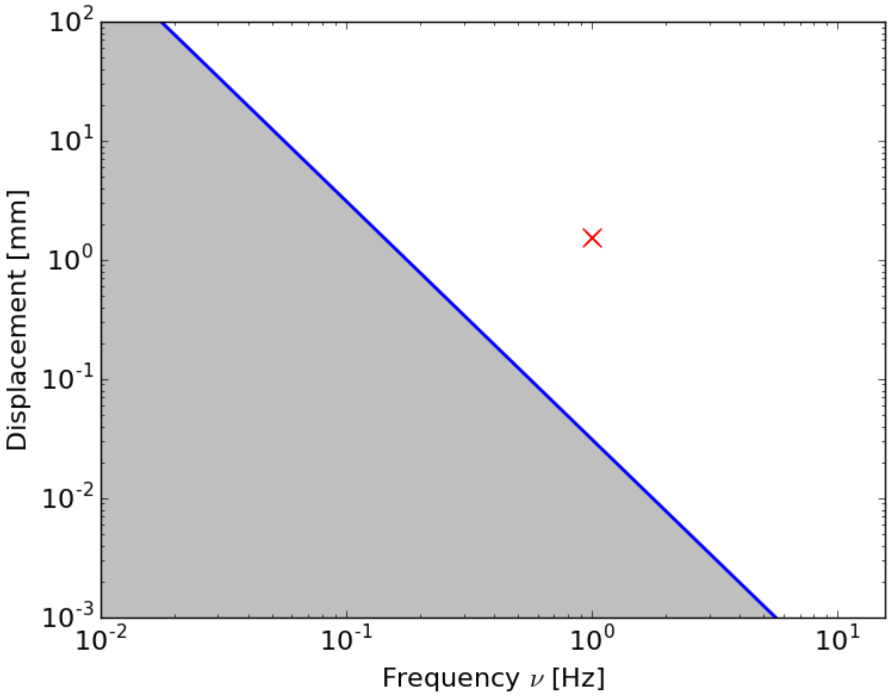

Figure 9: Noise induced limit on detectable oscillation amplitudes as a function of frequency. The red cross indicates the initial estimate for anticipated oscillations.

5. Analysis and Results

Data was taken on six different nights resulting in a total coverage of 51 h containing 83 H.E.S.S. observation runs, 60 of which were longer than 5 minutes. One measurement was performed for each of the five telescopes during normal observation procedure. Additionally, so-called pointing runs, where the telescopes point at various different objects in the sky in quick succession, were recorded with the sensor attached to the CT4 telescope. The analysis of the data was performed using *Python* with the *numpy* [30] and *scipy* [31] modules.

In the following chapters, the analysis methods and results from simulated and real data are presented.

5.1. Overview and understanding of general features

In order to understand the measurement results, the most prominent features present in the data need to be explained first. Fig.10(a) shows the entire uncalibrated data taken by the sensor while attached to the CT2 telescope. The measurement spans several runs performed over the entire night for different observed objects. The most prominent features are the large steps that can be seen mostly in the acceleration level of the y- and z-axis. Because the telescopes repeatedly change their pointing target, which in turn requires an adjustment of the altitude angle, the fraction of gravity measured in the y- and z-axis changes according to the dependencies given in chapter 3.5, while the x-axis remains largely uninfluenced because it is parallel to the altitude angle rotation axis and points along the horizon. This results in the steps seen in the graph whenever the target of observation is changed. It also explains the almost mirrored behaviour of these two axes, since the gravitational acceleration is simply shifted from one axis into the other. The steps can be observed in the x-direction as well, albeit with much smaller amplitude than their counterparts in the other axes. This is likely caused by a slight alignment error of the x-axis, causing it not to be perfectly perpendicular to the direction of gravity. This leads to a slight influence of the altitude angle on the fraction of gravity measured in the x-axis of the sensor, which would be zero for the case of ideal alignment.

The set of smaller steps in principle follows the same explanation, except for the fact that the observation target stays the same and only the pointing offset from the source is changed slightly, leading to much smaller movements of the telescopes. The offset typically changes by 1° in either right ascension or declination. Accompanying each step, a peak in acceleration can be observed, which is a result of the actual acceleration and deceleration the telescope experiences when the target or pointing offset is changed.

During an ongoing observation run, very little acceleration is expected to happen.

Therefore, the curve of the total acceleration is anticipated to show a flat line at 1 g with peaks whenever the pointing is altered and the telescope is rotated after a completed run. Since this is clearly not the case, the need to apply the previously discussed calibration becomes apparent. The total acceleration after incorporating these corrections is shown in Fig.10(b).

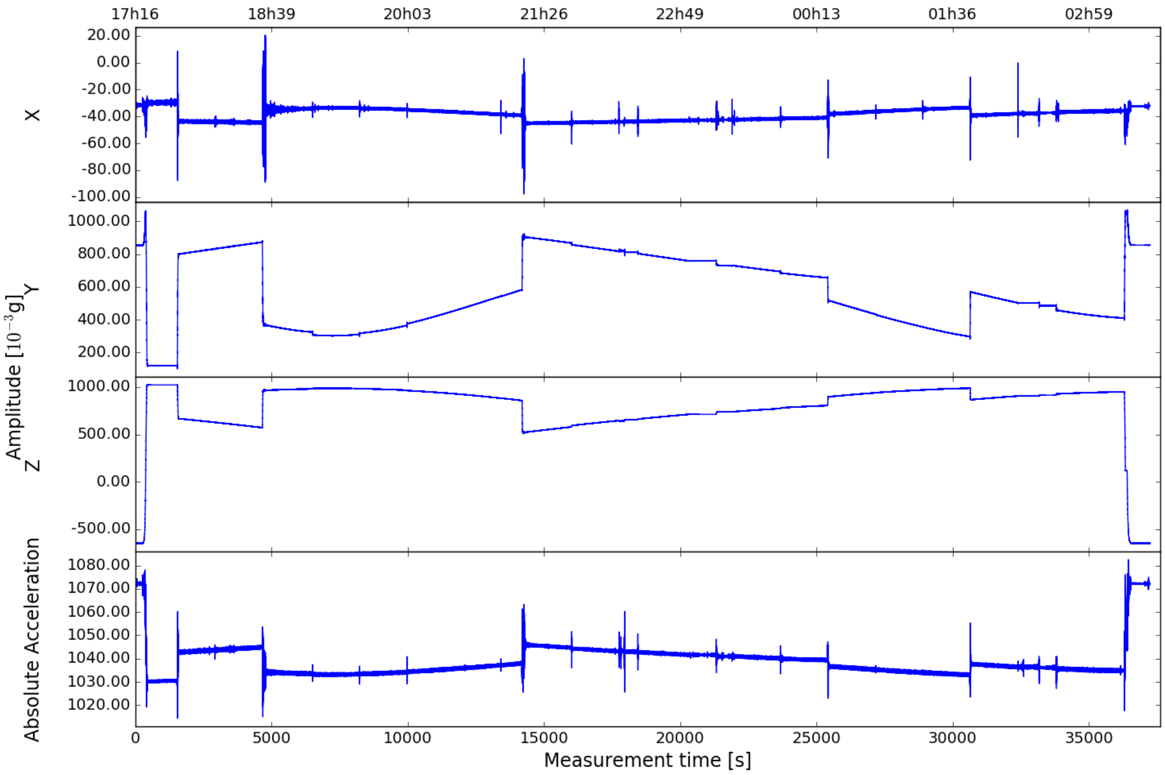

(a) Raw acceleration data

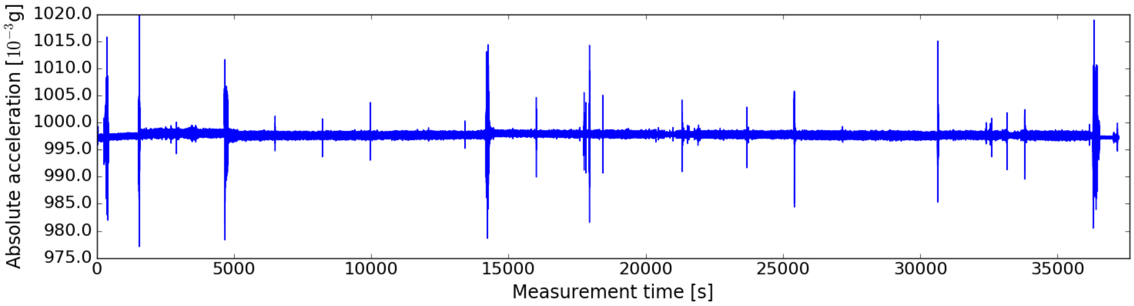

(b) Absolute acceleration after correction of zero-g offset and gain

Figure 10: Raw acceleration data measured at CT2 in all three axes along with the absolute value (a) and the absolute acceleration from the same measurement after applying the corrections from the calibration (b). The x-axis shows the time of the day at the top and the elapsed time in s at the bottom. Note the different acceleration scales for the measurements along the different axes.

Besides the expected peaks, the calibrated data shows very little time dependent change in the overall acceleration level. The average acceleration over the entire measurement is $997.7 \ \cdot 10^{-3}$g, which is slightly below the anticipated level. This can be explained by the difference in location for the calibration and the actual measurement. The acceleration due to gravity can vary between 9.78 $\mathrm{m/s^2}$ at the equator and 9.83 $\mathrm{m/s^2}$ at the north pole depending mainly on height and latitude [32]. Using the International Gravity Formula [33] and taking the height above sea level into account via the so-called free air correction [34] produces values for the gravitational acceleration of 9.78284 $\mathrm{m/s^2}$ for the H.E.S.S. site (Lat: $-23.271667°$, Height: 1800 m) and 9.80919 $\mathrm{m/s^2}$ for the location of the calibration near Erlangen (Lat: 49.61869°, Height: 380 m) (Values calculated via [35]). A division of these two values shows that after calibration in Erlangen, the sensor should detect $g_{H.E.S.S.} = 997.3 \ \cdot 10^{-3}$g at the H.E.S.S. site. Since the peaks in the actual signal were not removed or corrected prior to calculating the average, it can only be used as a rough estimate of the true value. However, it is still reasonably close to the theoretical expectation.

5.2. Analysis procedure

While considering the entire measurement yields a good overview of the acquired data, a closer and more in-depth look is necessary to investigate oscillations that could explain uncertainties in the telescope pointing. In order to do that, only excerpts of the data are used for analysis, most of which are contained inside single observation runs. The methods used to process and understand the data are explained in the following chapters.

5.2.1. Altitude angle correction

When tracing an object along the sky over the course of an observation run, the telescope's altitude angle has to be constantly adjusted. As explained before (see chapter 3.5), this changes the amount of gravitational acceleration acting upon the y- and z-axis of the sensor. Even though this only results in a slowly changing offset of the acceleration values superimposed upon the signal, it is important to distinguish these gravitational effects. Because gravity is compensated by the support structure of the camera, it won't lead to acceleration or movement of the camera. Therefore, the acceleration from gravity needs to be subtracted from the measured data before later on an integration can be performed to obtain the velocity and displacement from the acceleration signal. In order to apply this correction to every data point recorded during an observation run, a fit is performed for both y- and z-axis over the whole run assuming a linear progression of the altitude angle $\alpha(t) = \alpha_0 + t \cdot \alpha_1$. Inserting this into eq.(18) and eq.(19) and considering the altered g-value at the H.E.S.S. site yields the following fit functions:

$$g_y(t) = g_{H.E.S.S.} \cdot \cos\left(\alpha_0 + t \cdot \alpha_1\right) \tag{28}$$

$$g_z(t) = g_{H.E.S.S.} \cdot \sin\left(\alpha_0 + t \cdot \alpha_1\right) \tag{29}$$

These fits result in two independent estimates for $\alpha(t)$ which are then averaged and used to remove the effect of gravity in the y- and z-axis from the measurement. A comparison between the altitude angle obtained via this procedure and the target coordinates taken from the H.E.S.S. run data can be seen in Fig.11 for two subsequent runs.

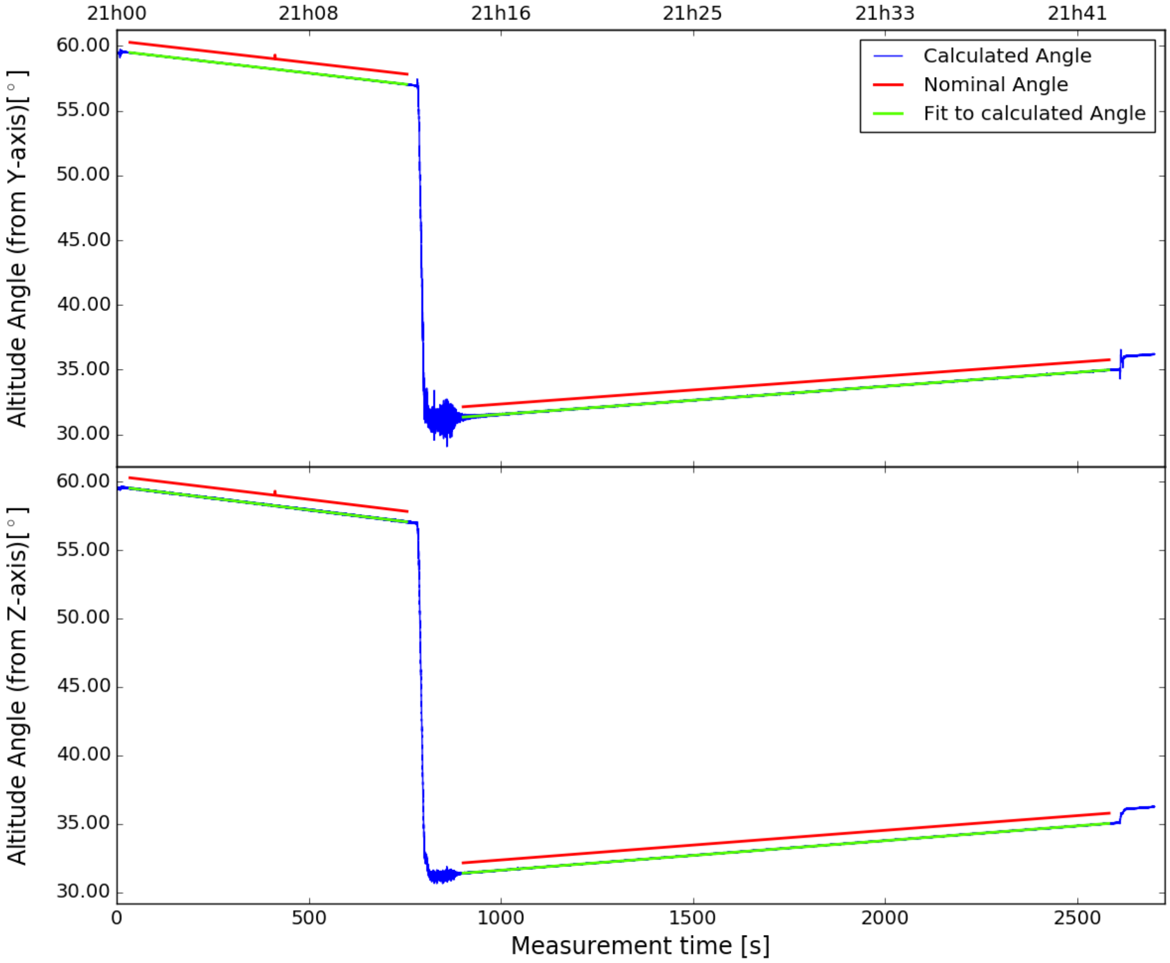

Figure 11: Comparison between a fit to the altitude angle obtained from the acceleration measurement at CT2 and the target coordinates of the runs. The blue curves show the calculated angle from the y-axis(top) and the z-axis(bottom) at every measurement point, the green lines are fits with linear altitude angle progression to the data and the red lines represent the values from the run documentation.

The measured angle and the documented value show the same qualitative behaviour with the slope α_1 differing by less than $5 \cdot 10^{-6}$deg/s. However, there is a small constant offset of 0.78° between calculated and documented angle. This is caused by a misalignment between the focal axis of the telescope and the z-axis of the sensor, which means that the device is rotated 0.78° around the x-axis compared to its ideal orientation. After the misalignment angle has been determined this way, the tracking data could in principle be used as well to compensate for the altitude angle effects.

5.2.2. Frequency representation of the signals

As the acceleration signal in the time domain can sometimes be difficult to interpret, changing to a different representation of the data can be helpful. Using a Fourier transform to express a time domain signal in terms of its frequency contents has the advantage that a complicated signal consisting of various oscillations with different frequencies can be decomposed into its periodic components. Here, the discrete variant of the Fourier transform is used since the obtained signal is not continuous but measured only at fixed points in time. Since the acceleration measurement utilizes to FIFO register of the ADXL355 to store data until it is saved (see chapter 3.3), it is ensured that the time between subsequent data points is fixed. Therefore, the Fourier transform can be performed via the Fast Fourier Transform (FFT) algorithm implemented through the *numpy.fft* module. The coefficients of the Fourier transform are given by [36]:

$$A_k = \sum_{m=0}^{n-1} a_m \exp\left(-2\pi i \frac{mk}{n}\right) \tag{30}$$

where n is the number of data points in the time series, a_m are the data points in the time domain and $k = 0, \ldots, n-1$. The inverse transformation is given by:

$$a_m = \frac{1}{n} \sum_{k=0}^{n-1} A_k \exp\left(2\pi i \frac{mk}{n}\right) \tag{31}$$

The absolute values $|A_k| = \sqrt{A_k \cdot A_k^*}$ of the Fourier coefficients yield the amplitude spectrum of the signal, while the power spectrum is given by the square of the absolute values $|A_k|^2 = A_k \cdot A_k^*$ (note: A_k^* denotes the complex conjugate of A_k). The amplitude spectrum of the acceleration data measured in the x-axis of the sensor during observation run 133746 after the altitude angle correction is shown in Fig.12 as a typical example. It can be seen that even above the internal low-pass filter cutoff frequency of the sensor at 15.625 Hz, features can be found in the Fourier spectrum, however, as will be shown later, these higher frequencies have a comparably small impact on the camera displacement (see eq.(42)).

While the Fourier representation can be used as a tool for analysis itself, it can also be helpful for understanding the influence that certain steps in the analysis procedure have on the frequency contents of the signal.

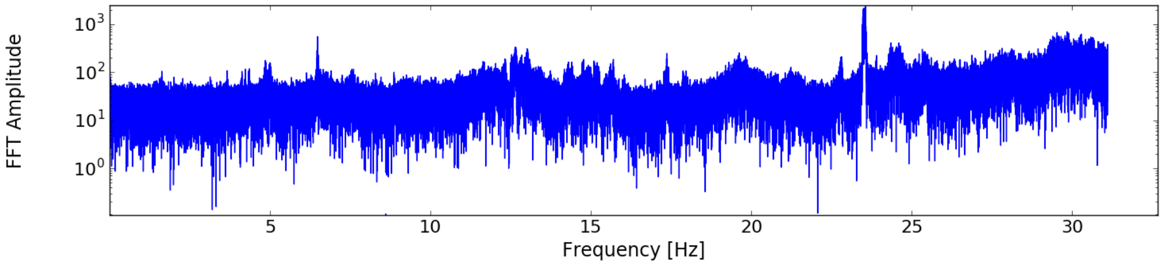

Figure 12: Fourier amplitude spectrum of the x-axis acceleration data during observation run 133746 after applying the altitude angle correction.

5.2.3. High-pass filtering

The signal that gets detected by the accelerometer is a superposition of all accelerating forces acting on the sensor during the measurement. Some of these signal components, such as the effects from tracking and gravity, are undesirable and need to be removed to ensure the validity of the results. Later on, the acceleration data will be integrated twice to calculate the displacement of the camera from its expected position. In order to do that, acceleration effects arising from a change of this expected position over time need to be compensated. Since the tracking of an object in the sky results in a movement of the camera on a sphere around the telescope, it can contribute to the acceleration signal (see. chapter 5.2.1). However, these effects are expected to happen on much longer time scales than those of the oscillations anticipated to be responsible for source widening and thus only contribute to the signal with rather low frequency components. A high-pass filter enables the removal of these low frequency contributions from tracking but also from other unwanted sources such as residual effects from gravity due to misalignment or other long-term changes in acceleration. Additionally, the filtering removes noise contributions below the cutoff frequency from the signal, which is useful since the low frequencies contribute the largest amount of noise to the displacement (compare Fig.9). The downside of the application of a filter is the reduction of the signal bandwidth. Ideally, the filter is chosen such that it is able to remove most of the unwanted low frequency portion of the signal while keeping the higher frequency part unchanged. To this avail, a digital Butterworth filter is used, which produces a maximally flat response in the passband region while causing less artefacts than a sharp frequency cutoff [37].

The frequency response of the Butterworth filter is shown in Fig.13(a) for different filter orders. The order of the filter does not only determine the strength of the cutoff in the frequency domain but also the step response of the filter in the time domain(see Fig.13(b)). The step response is the signal that is produced when the filter is supplied with a step function of unit height. The time it takes for the oscillation of the signal to drop below a given threshold is called settling time. It depends on the order of the filter as well as its cutoff. To avoid effects at the start and end of a measurement arising from the step response of the filter, the data is truncated by an amount equivalent to at least the settling time after the filter is applied. For the oscillation of a 4th order filter to drop below 0.01%, a time of 1.2 s is needed for a cutoff at 4 Hz and 9.2 s for a cutoff at 0.5 Hz.

In the following, a high-pass filter of 4th order with a cutoff at 0.5 Hz is used in the analysis, unless otherwise noted. This particular choice of parameters yields a good compromise between the necessary removal of unwanted low frequency contributions while keeping the impact on the frequency range above 1 Hz targeted in this investigation minimal and providing an acceptable settling time.

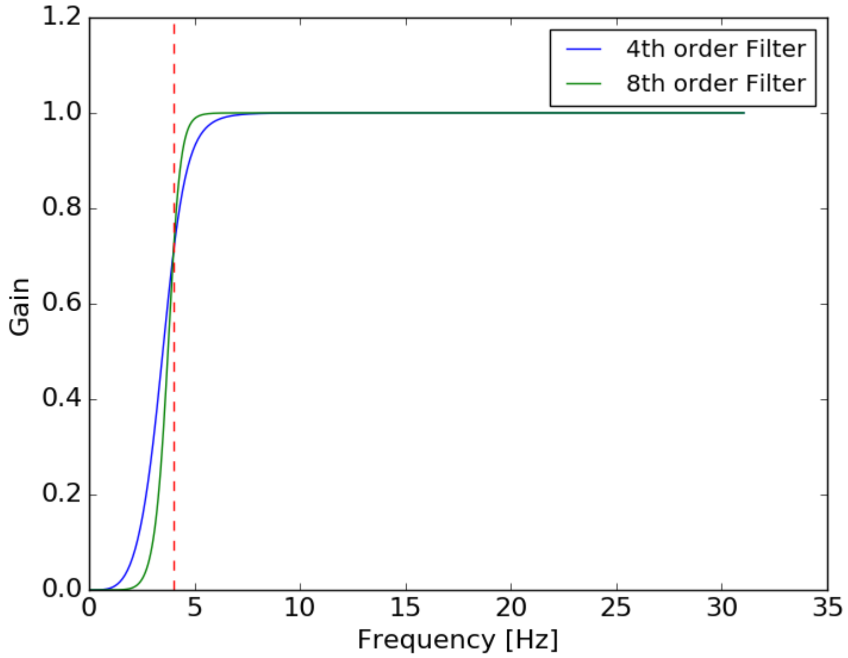

(a) Frequency response

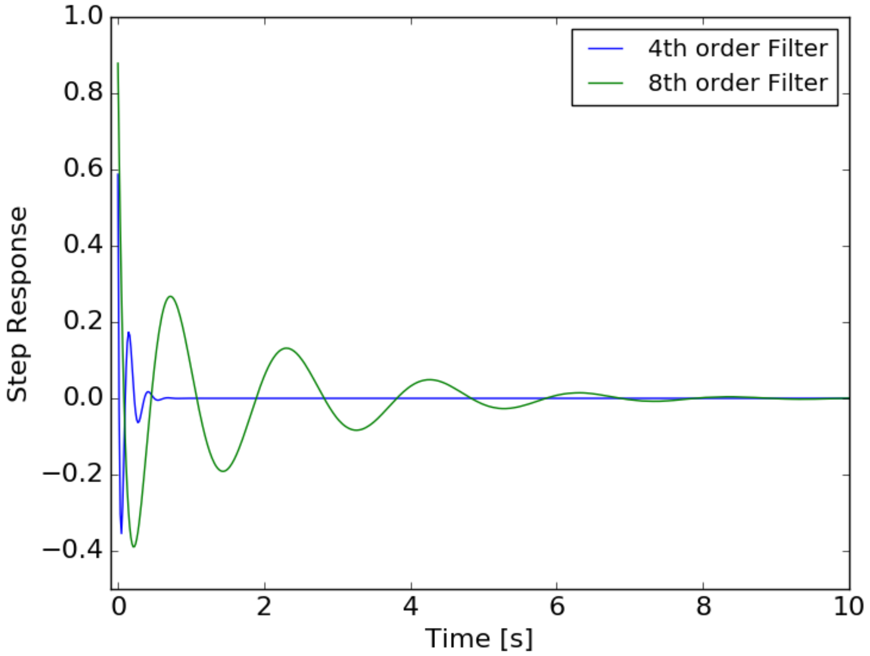

(b) Step response

Figure 13: Response function of a 4 Hz Butterworth high-pass filter in the frequency domain (a) and step response function in the time domain (b).

5.2.4. Obtaining displacement: Numerical integration

The displacement of the sensor can in principle be obtained via twofold integration of the measured acceleration data. The first integration yields the velocity of the camera at a certain time t. For a continuous acceleration $a(t)$ it is in general given by:

$$v(t) = v_0 + \int_{t_0}^{t} a(t')\,\mathrm{d}t' \tag{32}$$

Here, $v_0 = v(t = 0)$ is the starting velocity and t_0 is the start time of the measurement. However, the sensor produces only a discrete set of output values a_n sampled at the sampling frequency $f_S = 62.5$ Hz. It holds that $a_n = a(t = \Delta t \cdot n)$, where $\Delta t = \frac{1}{f_S}$ is the time between two samples. Integration of this discrete set of data points can be performed using the composite trapezoid rule. This method approximates the area under the graph between two points as a trapezoid [38]:

$$\int_{t}^{t+\Delta t} f(t')\,\mathrm{d}t' \approx \Delta t \cdot \left(\frac{f(t) + f(t+\Delta t)}{2}\right) \tag{33}$$

Therefore, the set of velocities can be written as:

$$v_m = v\left(t = \Delta t \cdot \left(m + \frac{1}{2}\right)\right) = v_0 + \Delta t \sum_{n=0}^{m} \frac{a_n + a_{n+1}}{2} \tag{34}$$

Note that because of the used method the set of velocities has one less entry than the measured samples ($m = 0, \ldots, n-1$) and is calculated at points in time between two acceleration data points. Since the sensor is fixed to the telescope camera, the starting velocity is set to $v_0 = 0$. A second integration with the same method yields a set of displacement values d_k:

$$d_k = d\left(t = \Delta t \cdot (k+1)\right) = d_0 + \Delta t \sum_{m=0}^{k} \frac{v_m + v_{m+1}}{2} \tag{35}$$

Here, d_0 is the starting position of the sensor which is again set to zero and the number of data points for the displacement is two less than the number of acceleration values. These integrations can be easily performed on a set of data, however, even a small offset can have a huge influence on the result. This can be understood when considering that an integration of a constant acceleration value of only $a(t) = 1\ \cdot 10^{-3}$g over a time period of one minute already yields a displacement of over 17 m. Thus it is important to properly prepare the data before the integration is performed or apply proper filtering afterwards.

5.2.5. Obtaining displacement: Omega arithmetic

Besides the direct integration in the time domain, there is another method that can be used to obtain the displacement. The so-called omega arithmetic utilizes the relationship between acceleration and displacement in the frequency domain [39]. First, displacement $d(t)$ and acceleration $a(t)$ are expressed in terms of their Fourier transforms $D(\omega)$ and $A(\omega)$:

$$d(t) = \int D(\omega) \cdot \exp(i\omega t)\, \mathrm{d}\omega \tag{36}$$

$$a(t) = \int A(\omega) \cdot \exp(i\omega t)\, \mathrm{d}\omega \tag{37}$$

Since the acceleration is the second derivative of the displacement, inserting eq.(36) into $a(t) = \ddot{d}(t) = \frac{\mathrm{d}^2}{\mathrm{d}\,t^2} d(t)$ yields:

$$\begin{aligned} a(t) &= \frac{\mathrm{d}^2}{\mathrm{d}\,t^2} d(t) && (38) \\ &= \frac{\mathrm{d}^2}{\mathrm{d}\,t^2} \left(\int D(\omega) \cdot \exp(i\omega t)\, \mathrm{d}\omega \right) && (39) \\ &= \int \frac{\mathrm{d}^2}{\mathrm{d}\,t^2} D(\omega) \cdot \exp(i\omega t)\, \mathrm{d}\omega && (40) \\ &= \int -\omega^2\, D(\omega) \cdot \exp(i\omega t)\, \mathrm{d}\omega && (41) \end{aligned}$$

By comparing eq.(41) and eq.(37) it can be seen that:

$$D(\omega) = -\frac{A(\omega)}{\omega^2} \tag{42}$$

This means that by computing the Fourier transform of the measured acceleration data, dividing by the factor $-\omega^2$ and then returning to the time domain by means of the inverse Fourier transform, the displacement can be obtained [40]. This furthermore shows that the periodic signal components of the displacement scale inversely with the square of their frequency. Because of this, it is clear that the displacement is dominated by components of low frequency while higher frequency portions of the signal get attenuated in the integration. Therefore, again the need to properly process the data in order to obtain meaningful results can be seen.

5.2.6. Displacement of simulated data

In this chapter, the analysis routine will be tested on a simulated and therefore well known signal. First, a suitable set of artificial data needs to be produced. This is done by superposition of different signal components. A constant baseline of acceleration values with the appropriate noise is produced by drawing random samples from a normal distribution with a width equal to the noise in the corresponding axis. The simulated noise for this is given by the average of the noise levels observed during the calibration measurements (see table 6).

This simple signal without any oscillation contribution can already be helpful to interpret the analysis results. By performing the same analysis that will later be used for real data on the artificial values, the contribution and effects from the accelerometer noise can be estimated. It is important to note that the corrections presented in chapter 4 are not applied in these simulations, since the noise values from the underlying calibration data were already corrected. The artificial data set is integrated via either of the previously discussed methods (numerical integration in the time domain or omega arithmetic in the frequency domain) and filtered with a Butterworth high-pass filter.

As expected, the distribution of the obtained displacement values follow a normal distribution. The width of this distribution is equivalent to the RMS displacement and depends on the used filter cutoff as is depicted in Fig.14 for a noise level equivalent to that of the x-axis of the accelerometer.

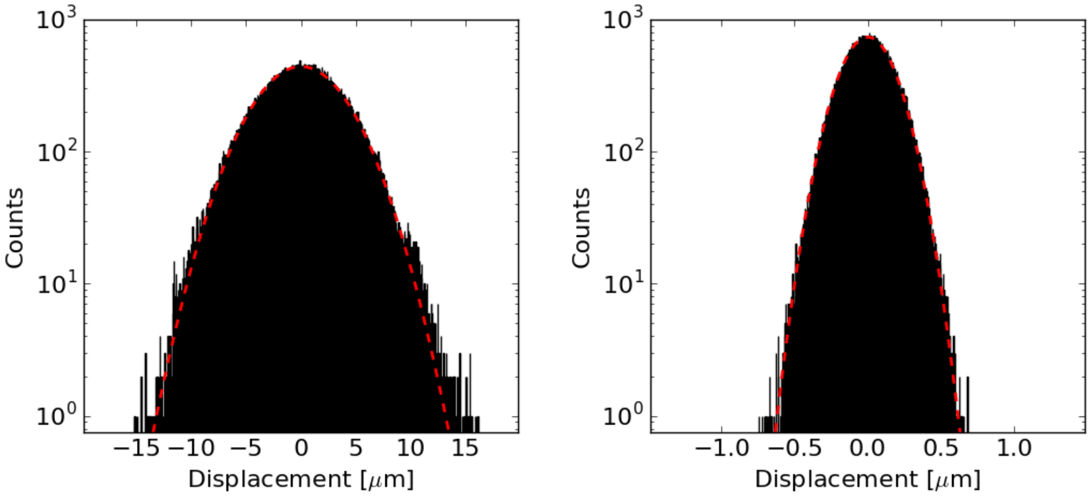

(a) Cutoff: 0.5 Hz (b) Cutoff: 4.0 Hz

Figure 14: Distribution of simulated displacement due to sensor noise using different high-pass filter cutoff frequencies.

The widths of the gaussian distributions obtained from the artificial data via both integration methods are given in table 7 for assumed noise levels equivalent to those measured in the respective sensor axis (compare chapter 4.3). The simulation was conducted for both high-pass filter cutoff frequencies. It can be seen that the different integration methods yield very similar results.

0.5 Hz Cutoff	Numerical integration	Omega arithmetic
X	3.9	3.9
Y	3.8	3.8
Z	7.9	7.9
4.0 Hz Cutoff		
X	0.16	0.17
Y	0.16	0.17
Z	0.33	0.35

Table 7: Width of the gaussian displacement distribution from simulations of the sensor noise in each axis, depending on the choice of high-pass filter cutoff frequency.

If the displacement calculated from a real data set follows the same distribution as in the simulations, the measurement is most likely dominated by noise, whereas a strong deviation from the simulated behaviour indicates the presence of effects leading to additional displacement beyond the noise contribution of the sensor.

Another aspect that can be investigated with the help of simulations is the effect of the analysis procedure on different initial signals. For this purpose, sinusoidal oscillations with different amplitudes and frequencies are added to the artificial data. The amplitude of the acceleration signal depends on the amplitude A and angular frequency $\omega = 2\pi\nu$ of the oscillation (see eq.(5)). The added acceleration signal component has the form:

$$a_{\text{osc.}}(t) = A \cdot \omega^2 \sin\left(\omega \cdot t\right) \tag{43}$$

The theoretical RMS displacement of such an oscillation is given by $d_{\text{RMS, theo.}} = \frac{A}{\sqrt{2}}$. The RMS displacement d_{RMS} recovered from the analysis with omega arithmetic is shown in table 8 for different combinations of oscillation amplitude and frequency alongside the corresponding expected value $d_{\text{RMS, theo.}}$.

The simulations show a good agreement with the theoretical values as long as the oscillation frequency ν is larger than the filter cutoff of 0.5 Hz and the theoretical RMS displacement is larger than the RMS displacement due to sensor noise (given in table 7). This highlights again the influence of the choice of filter cutoff frequency since a higher threshold frequency means a lower noise level and thus the ability to detect oscillations with smaller amplitudes but with the tradeoff of losing the sensitivity to lower frequencies.

Frequency ν[Hz]	A[µm]	d_{RMS}[µm]	$d_{\mathrm{RMS,\ theo.}}$[µm]
1	100	70.5	70.7
1	10	8.0	7.1
1	5	5.3	3.5
10	1	4.0	0.7
10	10	8.0	7.1
0.4	100	10.9	70.7
0.4	10	4.0	7.1
0.3	100	4.0	70.7

Table 8: Root-mean-square displacement obtained from the analysis of simulated oscillations with different parameters using omega arithmetic and a 0.5 Hz filter cutoff. Also shown are the calculated theoretical values of the RMS displacement.

In the cases where the oscillation amplitude and frequency are in the region where a detection is possible, the distribution of displacement values differs from a normal distribution. The effect is stronger for larger oscillation amplitudes. This is depicted in Fig.15 for an oscillation with frequency 1 Hz. Additionally, the Fourier representation of the displacement data shown in Fig.16 clearly shows a peak at the frequency of the oscillation.

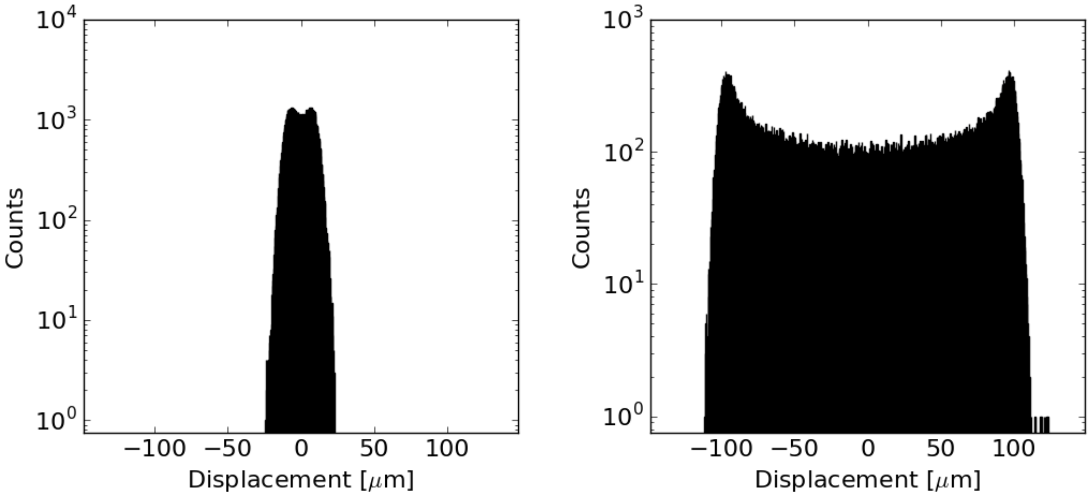

(a) Amplitude 10 µm

(b) Amplitude 100 µm

Figure 15: Distributions of displacement values from simulations of a sinusoidal oscillation with frequency 1 Hz and amplitudes of 10 µm (a) and 100 µm (b) respectively. An increasing deviation from a gaussian distribution can be seen for increasing oscillation amplitudes.

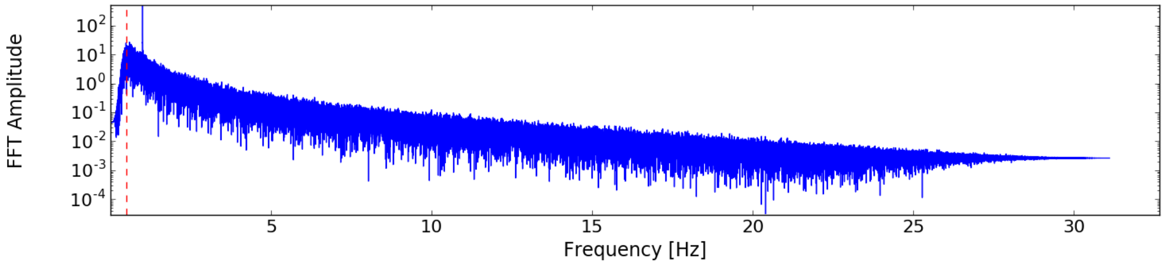

Figure 16: Fourier representation of the displacement signal from a simulated oscillation with frequency 1 Hz and amplitude 10 µm and simulated noise.

5.2.7. Displacement during a real measurement

In this chapter, the analysis procedure to obtain the camera displacement is showcased on the example of the data obtained for the CT2 telescope during run 133746. The measured and calibrated acceleration data from the run is shown in Fig.17(a) and the corresponding Fourier amplitude spectrum is depicted in Fig.17(b).

The first step is the removal of the contribution of gravity which is measured by the sensor but does not actually lead to an acceleration of the camera. This is done by applying the altitude angle correction presented in chapter 5.2.1 to the y- and z-axis measurement. Additionally, a linear fit to the x-axis data is performed and subtracted to eliminate possible gravity contributions, e.g. due to misalignment. This mainly influences the low frequency contents of the signal as can be seen by comparing the Fourier spectra shown in Fig.17(b) and Fig.18, which were calculated before and after the altitude angle correction respectively.

After this, the corrected data is integrated twice to obtain the displacement of the camera. As previously described, this can be done either in the time domain by numerical integration or in the frequency domain using the omega arithmetic. However, the result of this integration does not only represent the displacement caused by oscillations but by a multitude of different effects. When looking at the integration in terms of the omega arithmetic (eq.(42)), it becomes clear that the low frequency portion of the signal has a much stronger influence on the displacement than higher frequencies because the Fourier coefficients are scaled by a factor of $\frac{1}{\omega^2}$. From the Fourier representation of the displacement signal along the z-axis (obtained using omega arithmetic), shown in Fig.19(a), it can be seen that the low frequency components dominate over the higher frequencies.

Since the goal is to investigate oscillations around the camera's nominal position, the total displacement over the course of a run should be close to zero since the camera is mostly fixed in place and only rather small movements can occur. To properly visualize

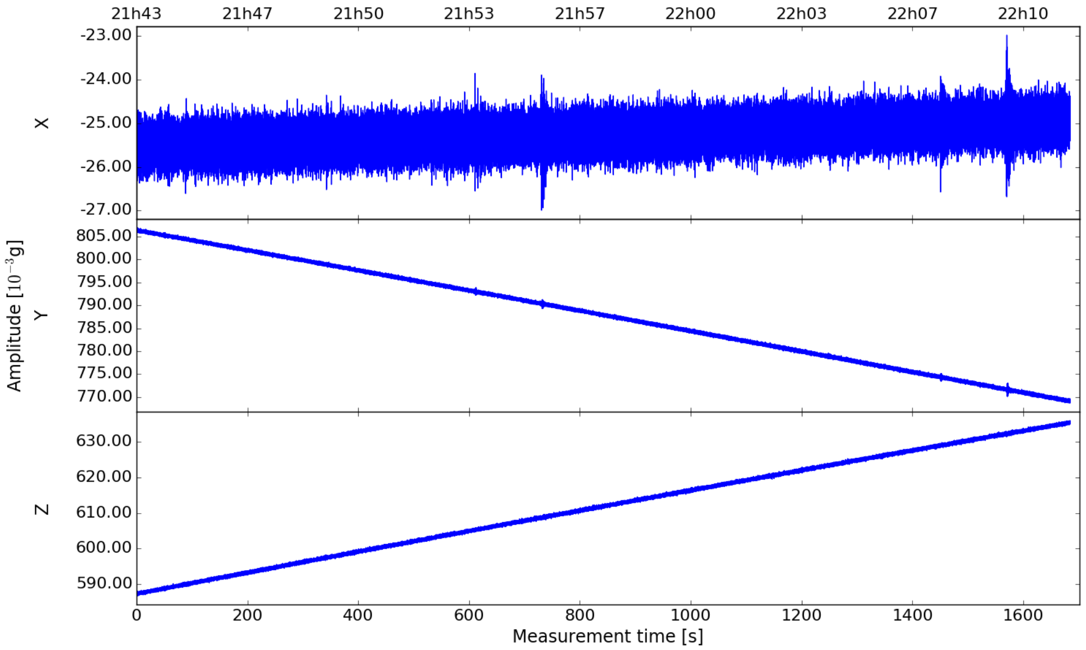

(a) Acceleration data from CT2. Note the different acceleration scales for the measurements in x-, y- and z-direction respectively

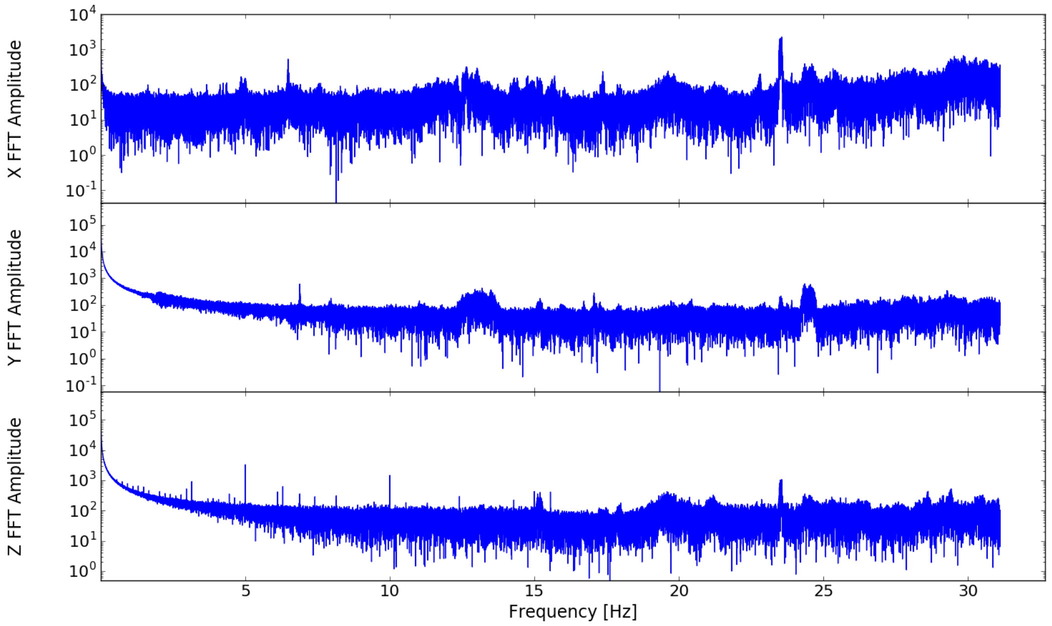

(b) Fourier amplitude spectrum of the acceleration data from CT2

Figure 17: Acceleration data (a) and the corresponding Fourier amplitude spectrum (b) measured at the CT2 telescope camera during run 133746.

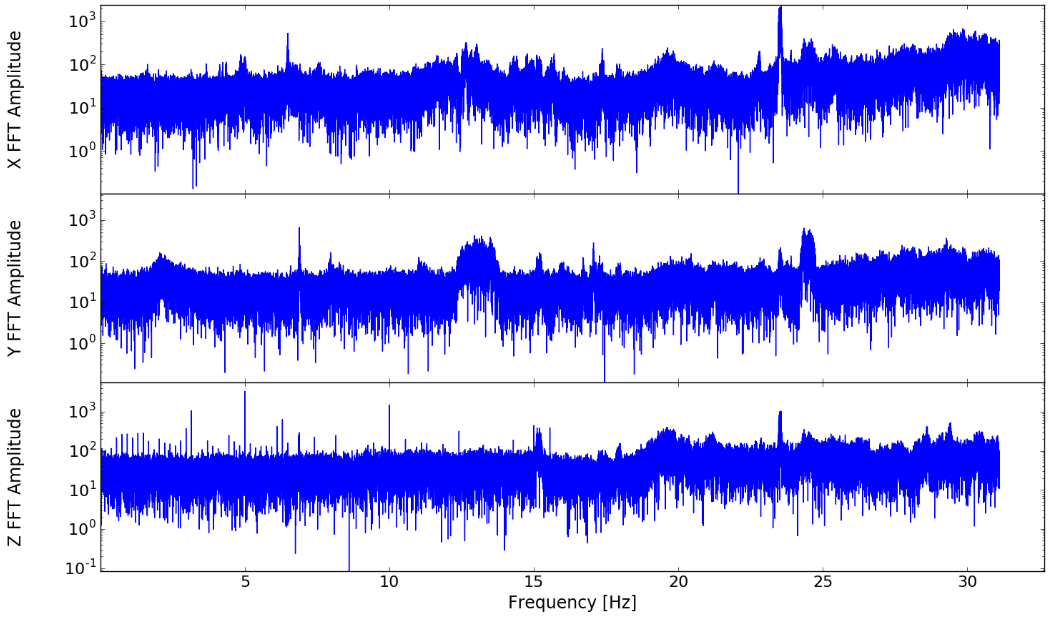

Figure 18: Fourier amplitude spectrum of the acceleration data from CT2 during run 133746 after angle- and linear fit corrections.

this, the low frequency components are removed from the signal using the Butterworth high-pass filter of 4th order with a cutoff frequency of 0.5 Hz as presented in chapter 5.2.3. This prevents a drift of the displacement over time that would render small scale effects invisible. The resulting displacements are shown in Fig.19(b) and 20(a) for the numerical integration and the omega arithmetic respectively.

Both methods produce similar results showing very little displacement and no significant features over the course of the measurement. By adjusting the high-pass filter to a cutoff frequency of 4.0 Hz, the bandwidth of the signal gets reduced, leading to a decrease in noise level. Therefore, some features in the form of sharp peaks in the displacement that were previously covered by noise are exposed (see Fig.20(b)) at the cost of hiding possible effects with lower frequency contributions. Since these displacement peaks are small and non-periodic, they most likely originate from a force acting on the sensor once e.g. caused by a small bump in the rail responsible for rotating the telescope during tracking.

The duration of an observation run covers a great number of periods of the anticipated oscillations. Therefore, the events detected over the course of a run happen at various camera displacements up to the oscillation amplitude. Thus, the effects on an image produced from such a run depend mostly on the RMS displacement of the camera and little on the frequency of the actual oscillation. The RMS displacement is obtained by calculating the standard deviation of the displacement values. For the CT2 camera during run 133746, the results are shown in table 9 for the different integration methods and filters. The results from both integration methods are again in relatively good agreement,

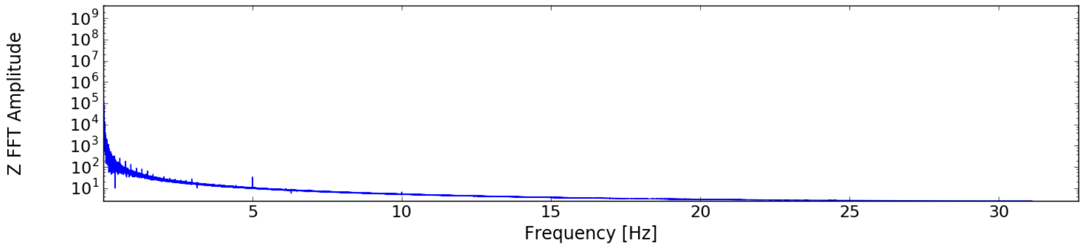

(a) Fourier amplitude spectrum of the displacement of the CT2 telescope camera along the z-axis before high-pass filtering

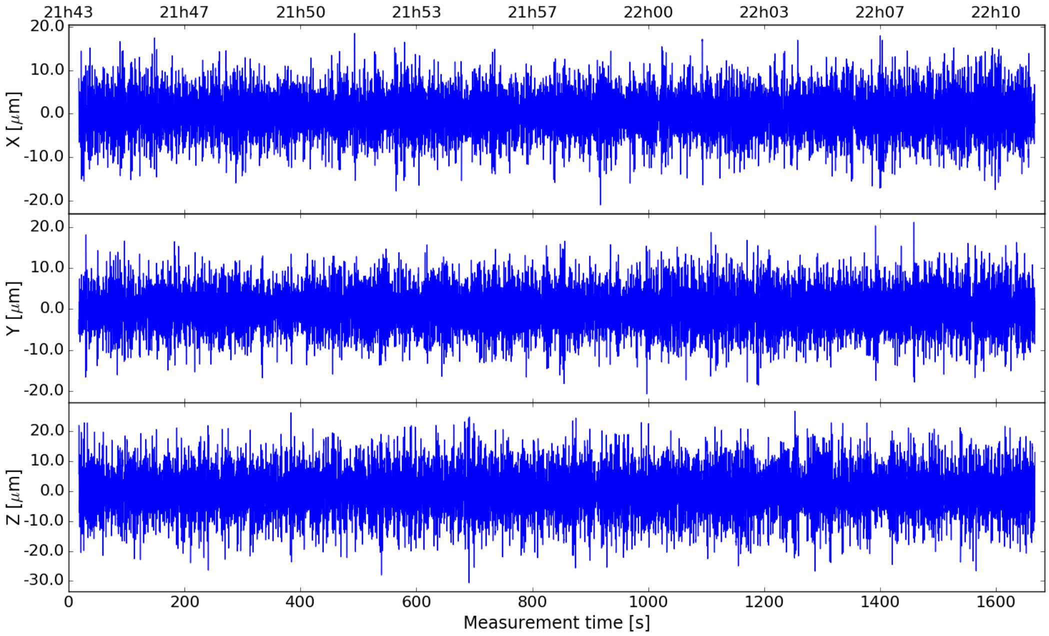

(b) Displacement of the CT2 telescope camera

Figure 19: Fourier spectrum (a) of the CT2 camera displacement along the z-axis during run 133746 showing the dominance of lower frequencies and the actual camera displacement (b) obtained through numerical integration and application of a Butterworth high-pass filter.

however, there is a big discrepancy between the two investigated cutoff frequencies. This is due to the different amount of noise that gets removed depending on the applied filter. To clarify the impact of the noise, the entire analysis procedure was repeated with simulated data. For this, artificial data was produced, using the average acceleration during the measurement in each axis as a baseline and adding a noise contribution. The noise was simulated equivalent to the procedure described in chapter 5.2.6 by drawing random samples of a normal distribution with width equal to the sensor noise measured in chapter 4.3. The resulting displacements are shown alongside the values for real data from run 133746 in table 9.

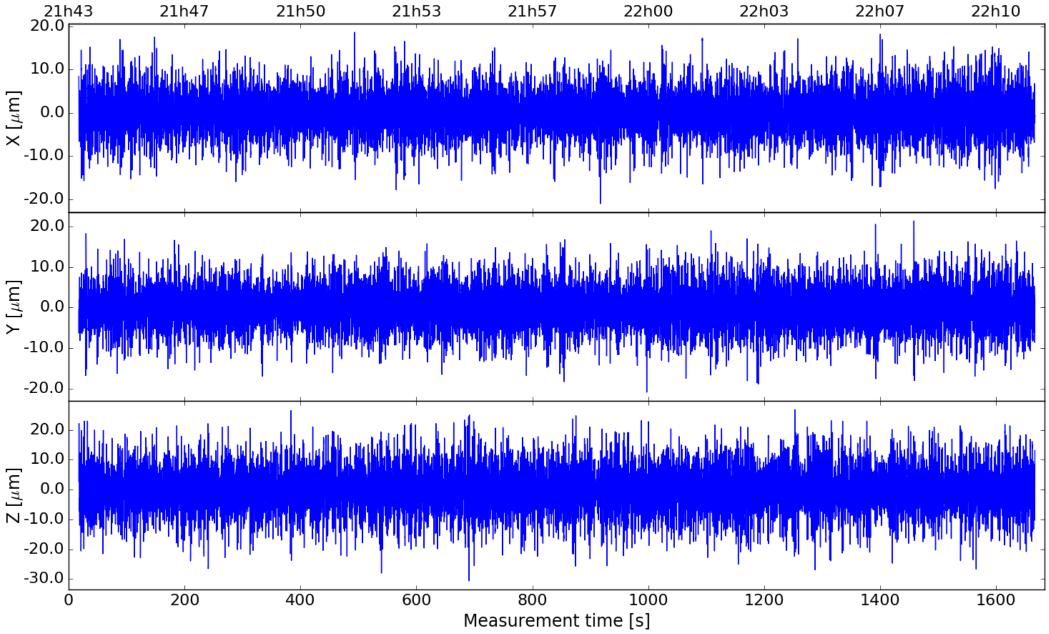

(a) Displacement with filter cutoff 0.5 Hz

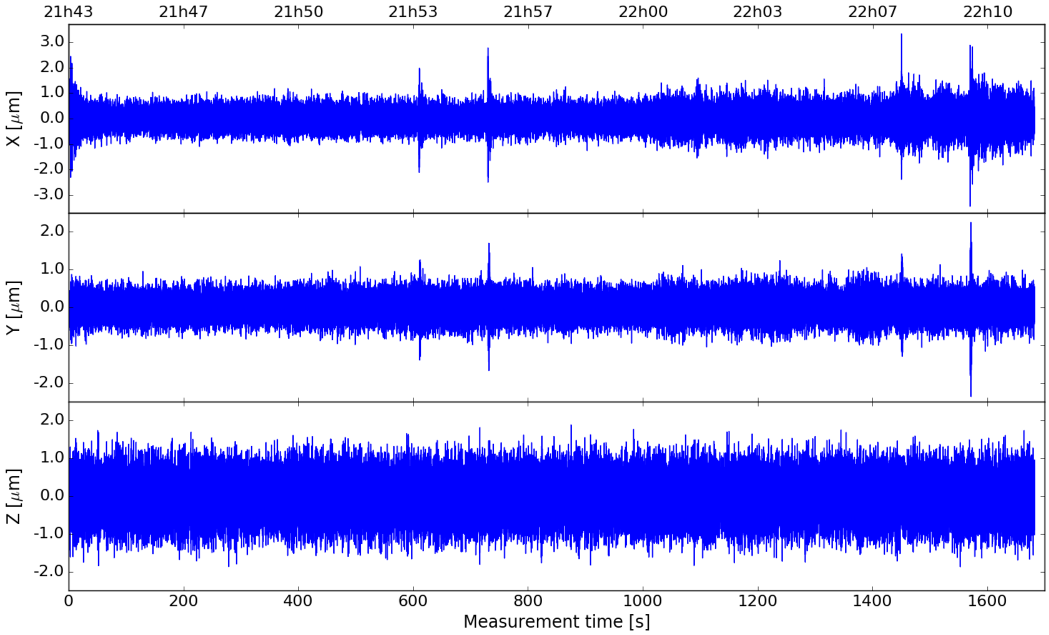

(b) Displacement with filter cutoff 4.0 Hz

Figure 20: CT2 camera displacement during run 133746 obtained through omega arithmetic and application of a Butterworth high-pass filter with 0.5 Hz (a) and 4.0 Hz (b) cutoff frequency respectively.

0.5 Hz Cutoff	Numerical integration	Omega arithmetic
X	4.9 (3.9)	4.9 (3.9)
Y	5.0 (3.8)	5.1 (3.8)
Z	7.7 (7.9)	7.7 (7.9)
4.0 Hz Cutoff		
X	0.33 (0.17)	0.38 (0.17)
Y	0.25 (0.17)	0.28 (0.17)
Z	0.49 (0.35)	0.53 (0.35)

Table 9: Comparison of the RMS camera displacement during run 133746 from both integration methods after applying a high-pass filter with either 0.5 Hz or 4.0 Hz cutoff frequency. The values in brackets are results from simulations assuming only sensor noise (compare chapter 5.2.6). All values are given in units of µm.

A comparison of the RMS displacement from the measurement d_{RMS} to simulated data $d_{\mathrm{RMS,\ sim.}}$ shows an agreement in a range of $\Delta = \frac{d_{\mathrm{RMS}}}{d_{\mathrm{RMS,\ sim.}}} - 1 \leq \pm 35\%$ for the 0.5 Hz filter. The results when using a filter with stricter cutoff of 4 Hz on the other hand differ by up to 100% or more in the x-axis. The Δ-parameter can be utilized to find runs with potentially interesting behaviour without the need to individually look at every run.

Another interesting property is the distribution of the displacement values around the mean value. This can be visualized as a histogram plot. For a displacement signal that is dominated by noise, the expected distribution follows a normal distribution, therefore, a deviation from this behaviour can indicate the presence of oscillations or other sources of displacement. Fig.21 shows the distribution of displacement values for the previously investigated run 133746 and for run 133741, which was chosen because of the large value of Δ along the y-axis. Both runs were processed in the previously described manner using omega arithmetic and a filter cutoff of 0.5 Hz. Additionally, the expected distribution is shown, which was obtained by running the analysis procedure on an artificially produced data set with no contributions to acceleration except noise and a constant offset (see chapter 5.2.6 for more details).

The graph shows a good agreement between expectation and measurement for run 133746 but the behaviour of the second run deviates strongly from the expected behaviour in the x- and y-axis due to pure noise, showing a much weaker decline towards larger displacements. This is reflected in the graph of the displacement shown in Fig.22 which exhibits several large peaks in those two axes, showing that in this case true physical effects dominate over the noise.

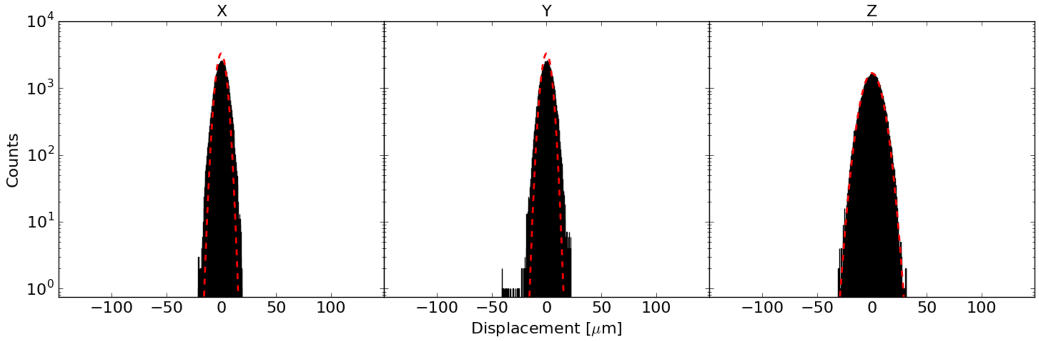

(a) Run 133746

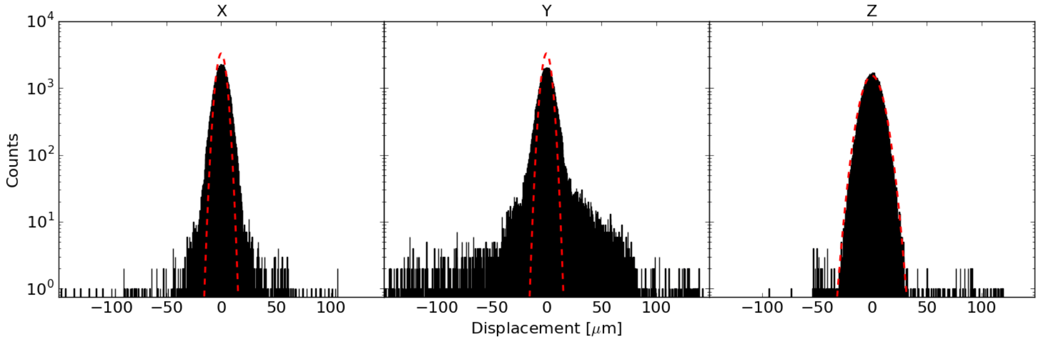

(b) Run 133741

Figure 21: Distribution of CT2 camera displacement values for different runs. The dashed red lines show the expected behaviour due to sensor noise. Run 133746 (a) is in good agreement with the prediction while the distribution from run 133741 (b) shows extended tails towards larger displacements.

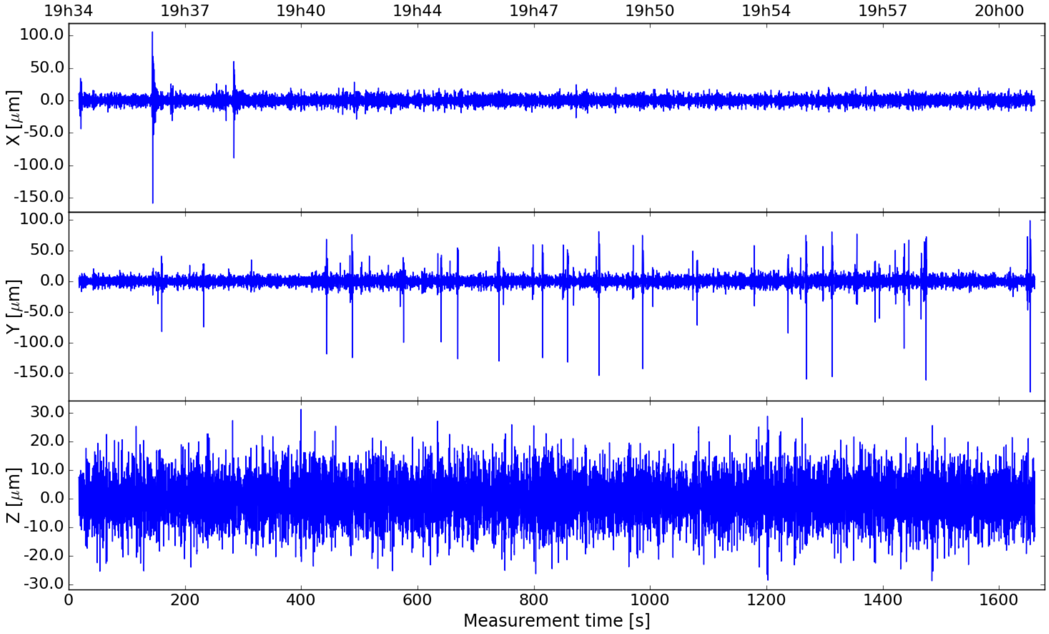

Figure 22: CT2 Camera displacement during run 133741 calculated using omega arithmetic. Several large peaks that dominate over the noise level can be seen in the x- and y-axis.

5.2.8. Results from a larger set of H.E.S.S. observation runs

In order to find observation runs that feature potentially interesting behaviour with a large displacement, the Δ-parameter is calculated for all runs during nights where the accelerometer was attached to the H.E.S.S. I telescopes. Runs where the Δ-value exceeds 100% in at least one axis are examined in terms of their time-dependent displacement and the distribution of this displacement value. This choice of the Δ-parameter corresponds to a deviation of over 100% in the RMS displacement between the simulated and measured results. A total of 14 runs are found that fulfill this criterion.

All of these runs result in histograms for the distribution of displacement values that differ strongly from simulated behaviour in either the x- or y-axis or both. On the other hand, for all investigated runs, the distribution in the z-axis is still in good agreement with the simulations. This can be explained by the orientation of this particular axis. Since the z-axis is parallel to the optical axis of the telescope, a displacement in this direction would require an elongation or compression of the camera support structure made of steel beams and therefore a very strong force. Because of this, the z-direction is extraordinarily stable compared to the other axes.

Two effects are found responsible for the large Δ-values. The first one can be seen in the y-axis data from run 133771 where the sensor was attached to CT3. The displacement, which is shown in Fig.23, shows several large peaks that lead to a larger than expected RMS displacement.

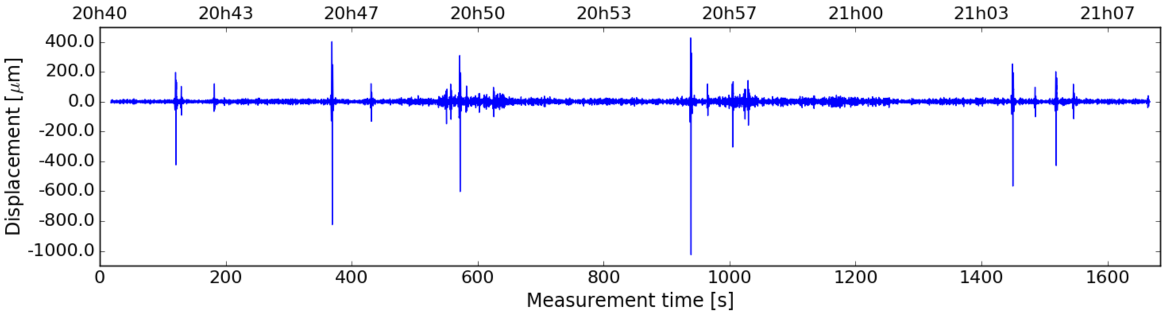

Figure 23: Displacement in y-direction of the CT3 camera during run 133771. Several large peaks can be seen, leading to a large RMS displacement.

The second type of measurement, where the root-mean-square displacement exceeds the predictions from the simulation, does not show singular features responsible for the effect. Instead, the displacement over the entire run is less stable than in the usual case, similar to an increase in the noise level. An example of this is given in Fig.24 which shows the y-axis of run 133787 again from CT3. This kind of effect could possibly be caused by wind on the H.E.S.S. observation site.

The difference between those two effects is also reflected in the distribution of their

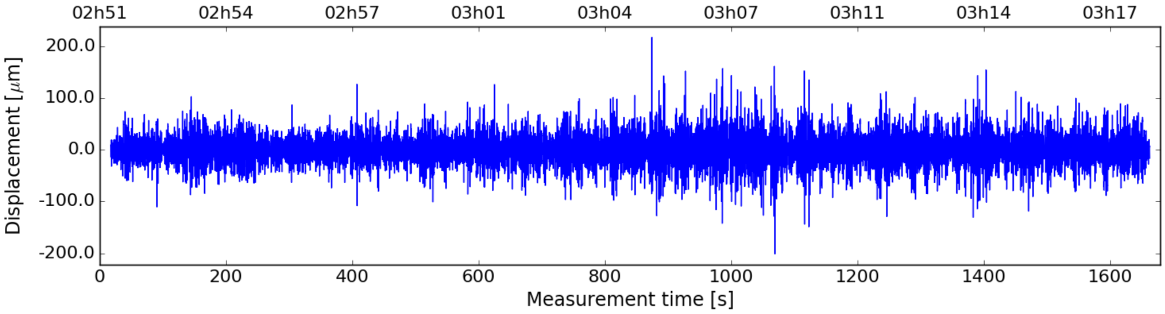

Figure 24: Displacement in y-direction of CT3 during run 133787. Showing rather large displacement values over the entire run, leading to a large RMS displacement.

displacement values. As shown in Fig.25(b), the distribution found for run 133787 shows a widening of the entire distribution. In contrast, the run where several peaks were detected shows a flattening of the distribution towards its edges in addition to producing a wider distribution than the simulations (see Fig.25(a)).

In order to estimate the magnitude of the impact these effects can have, the displacement values need to be corrected for the noise of the sensor. Under the assumption that the intrinsic distribution of the camera displacement over time follows a normal distribution, the measured distribution can be described as the sum of two gaussian distributions. With this, the width of the intrinsic distribution $d_{\text{RMS, int.}}$ can be calculated by:

$$d_{\text{RMS, int.}} = \sqrt{d^2_{\text{RMS}} - d^2_{\text{RMS, sim.}}} \tag{44}$$

Here, d_{RMS} is the RMS displacement from the acceleration measurement obtained via integration and high-pass filtering as described in chapter 5.2.7 and $d_{\text{RMS, sim.}}$ is the simulated value purely due to sensor noise (see chapter 5.2.6). While the simulated displacement from the noise contribution is certainly normally distributed (as is shown in chapter 5.2.6), this assumption is not necessarily true for the intrinsic displacement distribution, especially when it is caused by a sinusoidal oscillation. However, this method suffices for a rough estimate of the camera displacement. Table 10 shows the largest RMS intrinsic displacement among all runs for each of the four H.E.S.S. I telescopes.

Telescope	$d^{\text{max.}}_{\text{RMS, int.}}$ [μm]
CT1	5.0
CT2	10.8
CT3	28.3
CT4	14.2

Table 10: Largest value of the RMS intrinsic displacement among all examined H.E.S.S. I runs.

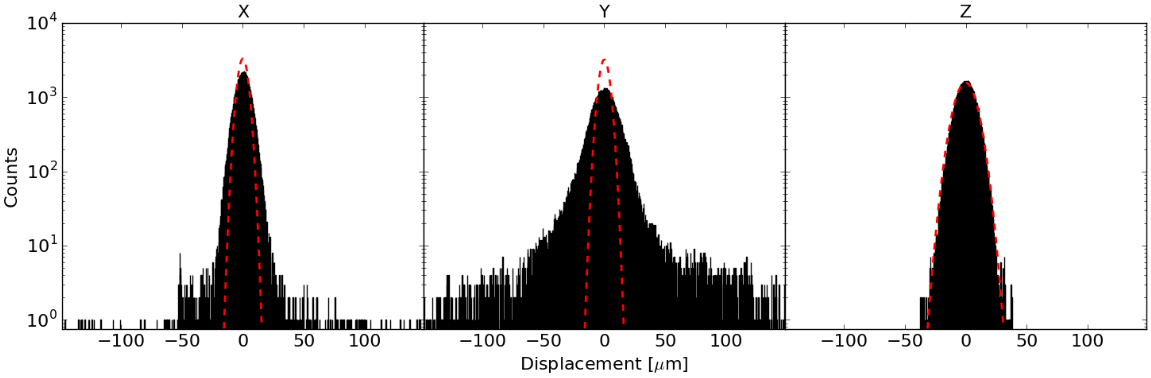

(a) Run 133771

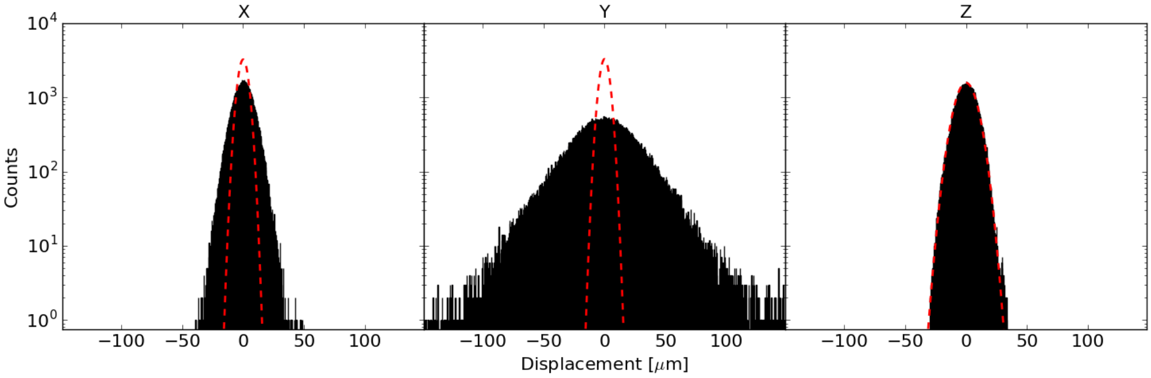

(b) Run 133787

Figure 25: Distribution of CT3 camera displacement values for different runs. The dashed red lines show the expected behaviour due to noise. Run 133771 (a) shows a widening of the x- and y-distributions compared to the simulations and a flattening towards the edges. Run 133787 (b) also shows a wider distribution than the simulations in those two axes. The z axis is in good agreement with the simulations for both runs.

Comparing these results to the initially suspected camera oscillation with a RMS displacement of over 1.0 mm shows that the measured effects are not sufficient to explain the pointing uncertainties of $\sigma = 15''$ even in the most extreme of observed cases. Furthermore, the cameras show a very stable behaviour with only minimal features during a majority of the recorded runs. The contribution from the RMS displacement to the pointing uncertainties $\sigma_{\text{disp.}}$ can be estimated by:

$$\sigma_{\text{disp.}} \approx \arctan\left(\frac{d^{\text{max.}}_{\text{RMS, int.}}}{D}\right) \tag{45}$$

With the focal length of the telescope $D = 15$ m. Even for the largest RMS displacement

$d^{\text{max.}}_{\text{RMS, int.}} = 28.3$ µm a contribution of only $\sigma_{\text{disp.}} = 0.39''$ is found.

Therefore, oscillation effects of the telescope cameras in the frequency range between 0.5 Hz and 15.625 Hz are most likely not the dominant source of pointing uncertainties.

5.2.9. Effects during pointing transitions

In this chapter, the effects occurring when a telescope changes its pointing target are investigated. The goal is to examine if a change of the pointing can impact the displacement of the run following directly afterwards. This could be the case if the time between the adjustment of the telescope direction and the start of the run is not sufficient for the camera to settle in place.

For this reason, the pointing transitions of the CT2 telescope are studied. As briefly mentioned before, two types of pointing changes can be distinguished. Small changes of typically 1° in right ascension or declination occur when only the pointing offset from an observed object is altered. In this case, the adjustment is expected to happen quickly because the telescope direction is only modified slightly, causing a small movement to be sufficient. On the other hand, the time it takes to switch to a different observation target altogether can be much longer depending on the angular distance between the previous and the new target.

In order to measure the duration for which a pointing transition influences a telescope, the absolute acceleration is considered. Because the telescope is accelerated during such a transition, a deviation from the otherwise almost constant behaviour of the absolute acceleration is expected. To find the start of a change in pointing, the standard deviation of the absolute acceleration within a certain time window is used. By finding the point where the standard deviation rises above a pre-defined threshold w.r.t. the normal value, the acceleration of the camera associated with the beginning of the movement can be identified. Analogously, the endpoint of the transition is reached when the standard deviation decreases below the threshold again.

A number of 30 samples was chosen to calculate the standard deviation and the threshold value was adjusted between 140% and 180% of the standard deviation from data points before the pointing transition, depending on the individual data set. This is shown in Fig.26 for the transition from the target ToO MAXI J1535-571 to PKS 2022-077. The starting point can be determined pretty accurately in most cases because of the abrupt start of the movement. However, it proves much more difficult to find the end of the pointing change influence because, rather than ending abruptly, it slowly decreases until it ultimately fades out. The durations of the pointing changes determined with this method are shown in table 11 together with the duration of the break in between the current and the next observation run. The time between two subsequent runs was obtained from the timestamp of the first detected event and the duration of each run, both of which were taken from the H.E.S.S. run database.

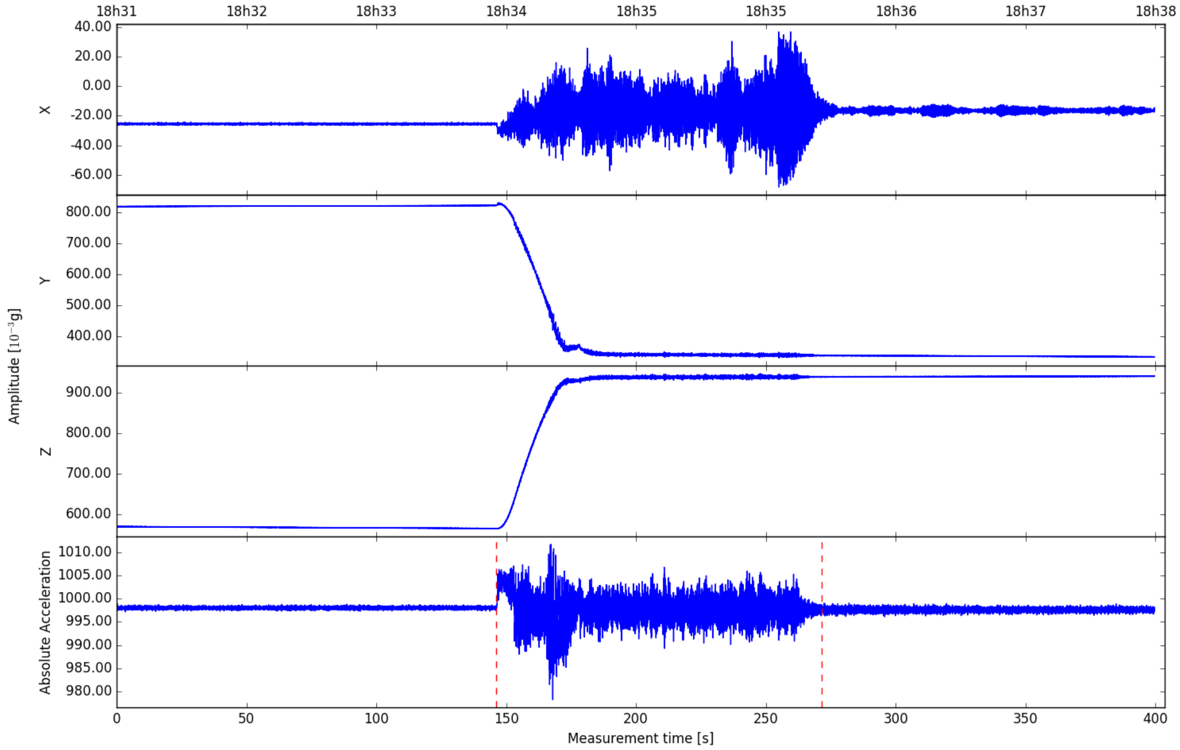

Figure 26: Acceleration measured during the pointing transition from the target ToO MAXI J1535-571 to PKS 2022-077. The dashed red lines show the period during which an increase in the standard deviation of the absolute acceleration is observed.

In principle, the duration of the break between two subsequent runs is sufficient to allow for a change in pointing without influencing the following measurement. However, since the transition towards a different target does not start immediately after a measurement is finished, the possibility that the telescope camera has not completely settled remains. From the investigated pointing transitions of CT2, one run in particular shows this behaviour. Fig.27(a) shows the measured acceleration data during the pointing transition from PKS 2022-077 to 3FGL J0244.8-5818 and also the start of observation run 133745.

It can be seen that in this particular case the run started too early for the camera to completely settle in place. Therefore, a small residual movement of the camera can be observed at the start of the run. This shows that it is possible for a pointing transition to influence the subsequent observation run at least in a some cases. To estimate the magnitude of these effects, the camera displacement is computed as described in chapter 5.2.7 but with the use of a 4.0 Hz high-pass filter cutoff instead of the usual 0.5 Hz. Fig.27(b) shows the RMS displacement, calculated by taking the standard deviation from 100 samples, as a function of time.

Large Transitions	Pointing Duration [s]	Time between Runs [s]
	123	165
	132	146
	31	85
	33	77
Small Transitions		
	10	46
	11	57
	14	50
	7	50
	11	47
	14	45
	5	46

Table 11: Comparison between the duration of the pointing transition, as determined from the absolute acceleration observed at the telescope camera and the corresponding break between observation runs.

It can be seen that the RMS displacement is still elevated at the start of the observation run and continues to decrease, approaching the level from before the start of the pointing transition. The RMS displacement reaches values up to 6.1 µm in the x-axis, 4.6 µm in the y-direction and 2.1 µm in the z-axis at the beginning of the observation run, whereas the values seen before the pointing transition are all considerably below 1.0 µm. While the resulting effects are small in this case, the possibility of such an error source should at least be considered.

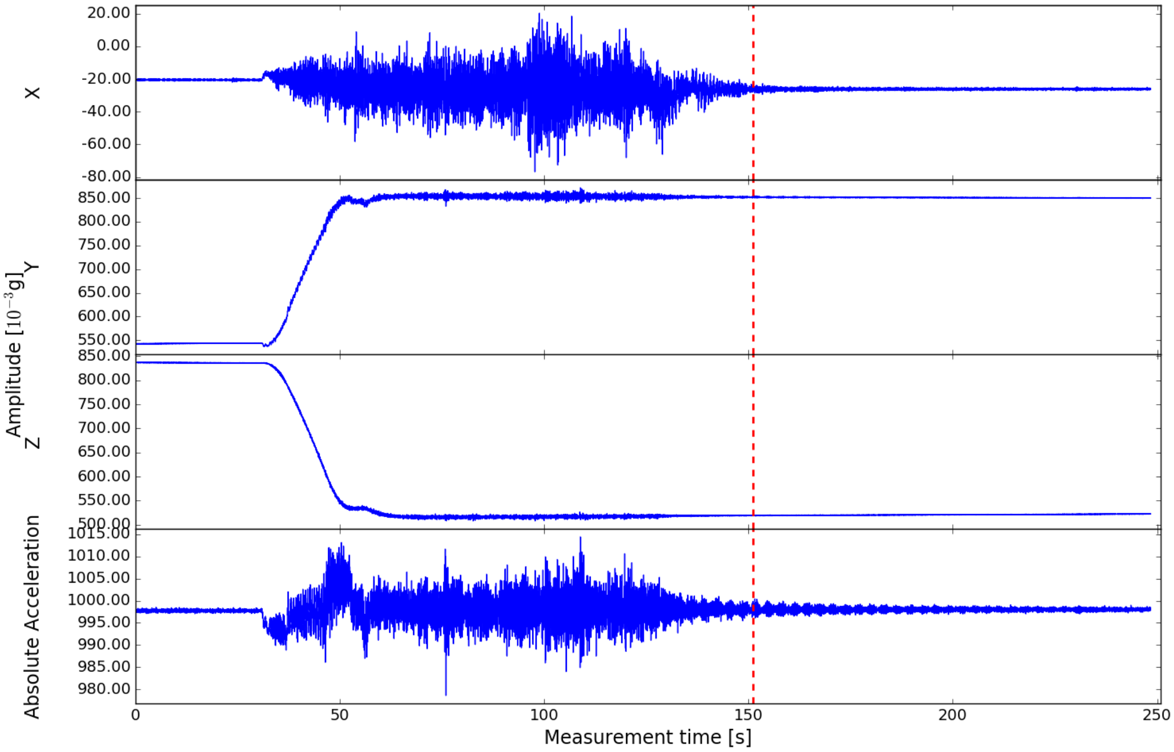

(a) Acceleration measured at the CT3 telescope camera

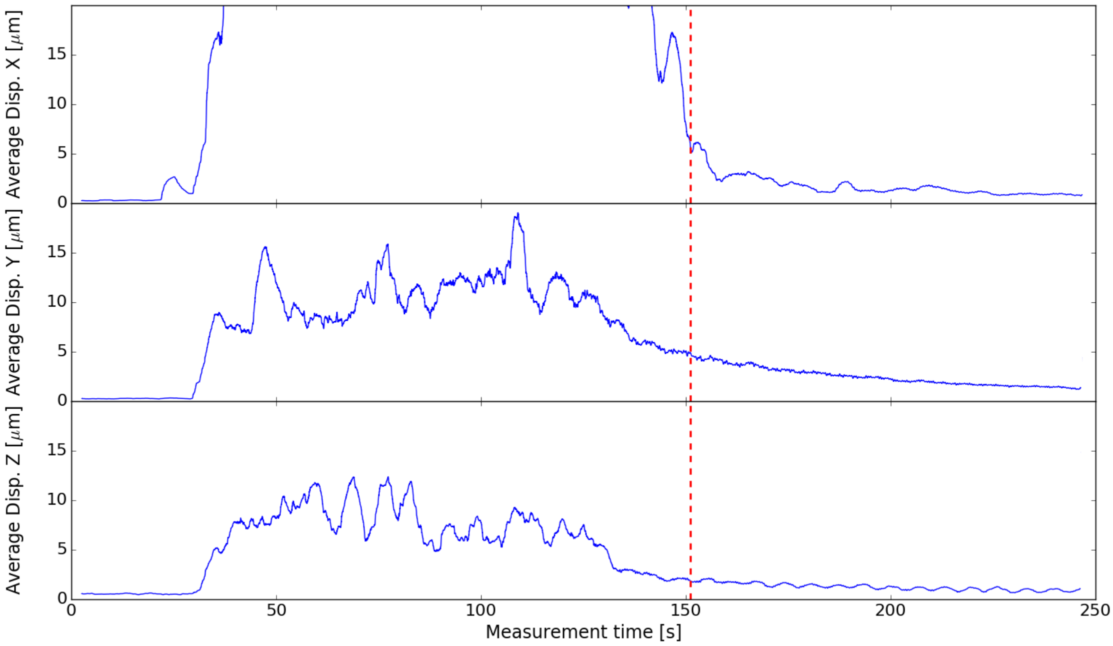

(b) RMS camera displacement calculated from the standard deviation of 100 data points

Figure 27: Acceleration (a) and RMS camera displacement from 100 data points (b) during the pointing change from PKS 2022-077 to 3FGL J0244.8-5818. The dashed red line shows the start of observation run 133745.

6. Conclusion

In this thesis, an investigation of suspected oscillations of the H.E.S.S. telescope cameras was performed by measuring the acceleration occurring at these cameras.

The sensor used in the measurements was designed, assembled and programmed in the scope of this work. It features an accelerometer as the main detection instrument, a programmable microcontroller as a control system and an SD-card to store the measured data as well as a GPS module for timekeeping. The sensor is able to operate independently of an external power supply due to the inbuilt power source.

A calibration of the most important sensor parameters, zero-g offset and gain, was performed and the intrinsic noise level of the device was determined and found compatible with the values stated in the accelerometer datasheet.

Real data from the H.E.S.S. site was taken for each telescope during one observation night. Additionally, a night of pointing runs was recorded for the camera of CT4. To obtain displacement values from the measured acceleration data, several steps are necessary. First, the altitude angle of the telescope was calculated from the data in order to correct for its influence. This calculation was compared to the tracking data during the same time period for an exemplary data set, revealing a very good agreement in the qualitative behaviour, only shifted by a small offset due to misalignment errors.

Subsequently, a twofold integration was performed to obtain the displacement. Two possible methods, one operating in the time domain and one in the frequency domain, were applied and found to produce comparable results. Lastly, a high-pass filter was applied to the displacement in order to reveal effects causing small displacements of the telescope camera from its nominal position and remove the influence of larger movements, e.g. due to tracking.

The analysis procedure was first tested on a set of simulated values in order to examine the influence of the intrinsic noise of the sensor as well as different filter parameters on the results. From this, the RMS camera displacement observed due to sensor noise was found as 3.9 µm along the x-axis, 3.8 µm in the y-axis and 7.9 µm in the z-direction of the device for a filter cutoff at 0.5 Hz.

Using the same analysis on the real data reveals a very stable behaviour during a majority of the runs. Specifically the axis parallel to the telescope's optical axis showed no major effects above the noise threshold, even though an effect was clearly visible in the other axes. This is attributed to its special orientation providing a larger rigidity due to the camera support structure. Looking explicitly into runs that showed a large RMS camera displacement revealed two types of origin for the displacement:

- Runs with one or multiple large peaks in the displacement
- Runs showing a general instability, similar to a larger noise level

Even with largest RMS camera displacement over an entire run of 28.3 μm, only a tiny fraction of the pointing uncertainties could be explained. Therefore, it was concluded, that oscillation effects of the cameras in the frequency range between 0.5 Hz and 15.625 Hz are most likely not the cause for the pointing uncertainties. This leaves either oscillations with different frequency components or an entirely different effect as feasible explanations.

Lastly, the effects from pointing transitions were investigated, revealing the possibility that a change in pointing direction can influence the subsequent run in certain cases. This effect was small for the investigated case, showing only a RMS displacement of 6.1 μm in the x-axis at the start of the run. However, the possibility of such an influence should not be neglected entirely.

List of Figures

List of Tables

References

[1] M. Holler et al. „Run-Wise Simulations for Imaging Atmospheric Cherenkov Telescope Arrays“ (Nov. 3, 2017). arXiv: `1711.01118v1 [astro-ph.HE]`.

[2] V. F. Hess. „Über Beobachtungen der durchdringenden Strahlung bei sieben Freiballonfahrten“. *Physikalische Zeitschrift 13* (1912), pp. 1084–1091.

[3] W. Hofmann and C. van Eldik. „Ein neues Fenster zum Kosmos. Gamma-Astronomie mit HESS“. *Sterne und Weltraum* (2009).

[4] C. Collaboration. „Search for dark matter in events with energetic, hadronically decaying top quarks and missing transverse momentum at $\sqrt{s} = 13$ TeV“ (Jan. 25, 2018). arXiv: `1801.08427v1 [hep-ex]`.

[5] E. Lorenz and R. Wagner. „Very-high energy gamma-ray astronomy: A 23-year success story in high-energy astroparticle physics“. *The European Physical Journal H: Volume 37, Number 3 (2012), 459-513* (July 25, 2012). DOI: `10.1140/epjh/e2012-30016-x`. arXiv: `1207.6003v1 [physics.hist-ph]`.

[6] S. Funk. „Space- and Ground-Based Gamma-Ray Astrophysics“ (Aug. 21, 2015). DOI: `10.1146/annurev-nucl-102014-022036`. arXiv: `1508.05190v1 [astro-ph.HE]`.

[7] F. M. Rieger, E. de Ona-Wilhelmi, and F. A. Aharonian. „TeV Astronomy“ (Feb. 22, 2013). arXiv: `1302.5603v1 [astro-ph.HE]`.

[8] K. Bernloehr et al. „The optical system of the H.E.S.S. imaging atmospheric Cherenkov telescopes, Part I: layout and components of the system“. *Astropart.Phys.20:111-128,2003* (Aug. 14, 2003). DOI: `10.1016/S0927-6505(03)00171-3`. arXiv: `astro-ph/0308246v1 [astro-ph]`.

[9] P. Hofverberg et al. „Commissioning and initial performance of the H.E.S.S. II drive system“ (July 17, 2013). arXiv: `1307.4550v2 [astro-ph.IM]`.

[10] S. Gillessen. „Sub-Bogenminuten-genaue Positionen von TeV-Quellen mit H.E.S.S.“ PhD thesis. Ruprecht-Karls-Universität Heidelberg, July 7, 2004.

[11] R. Cornils et al. „The optical system of the H.E.S.S. imaging atmospheric Cherenkov telescopes, Part II: mirror alignment and point spread function“. *Astropart.Phys.20:129-143,2003* (Aug. 14, 2003). DOI: `10.1016/S0927-6505(03)00172-5`. arXiv: `astro-ph/0308247v1 [astro-ph]`.

[12] P Vincent et al. „Performance of the H.E.S.S. cameras“ (July 2003).

[13] S. Funk et al. „The trigger system of the H.E.S.S. telescope array“. *Astroparticle Physics* 22.3-4 (2004), pp. 285–296. DOI: `10.1016/j.astropartphys.2004.08.001`.

[14] J. Bolmont et al. „The camera of the fifth H.E.S.S. telescope. Part I: System description“ (Oct. 22, 2013). DOI: `10.1016/j.nima.2014.05.093`. arXiv: `1310.5877v2 [astro-ph.IM]`.

[15] H. Stöcker. *Taschenbuch der Physik*. 6th ed. 2010.

[16] J. A. Hinton and W. Hofmann. „Teraelectronvolt Astronomy“. *Ann.Rev.Astron.Astrophys. 47:523-565,2009* (June 27, 2010). DOI: `10.1146/annurev-astro-082708-101816`. arXiv: `1006.5210v2 [astro-ph.HE]`.

[17] F Aharonian et al. „High energy astrophysics with ground-based gamma ray detectors“. *Reports on Progress in Physics* 71.9 (2008), p. 096901. DOI: `10.1088/0034-4885/71/9/096901`.

[18] K. Stycz. „VHE Gamma-Ray Sources at the Resolution Limit of H.E.S.S.“ PhD thesis. Humboldt-Universität zu Berlin, 2015.

[19] M. Holler et al. „Advanced search for the extension of unresolved TeV sources with H.E.S.S.: First measurement of the extension of the Crab nebula at TeV energies“ (July 13, 2017). arXiv: `1707.04196v1 [astro-ph.HE]`.

[20] M. Garczarczyk. *Medium-Sized Telescope Technical Design Report.* CTA Construction Project, 2016.

[21] E. W. Weisstein. *Root-Mean-Square.* From MathWorld–A Wolfram Web Resource. 2017. URL: `http://mathworld.wolfram.com/Root-Mean-Square.html`.

[22] Analog Devices. *Low Noise, Low Drift, Low Power, 3-Axis MEMS Accelerometers ADXL354/ADXL355.* 2016. URL: `http://www.analog.com/media/en/technical-documentation/data-sheets/ADXL354_355.pdf`.

[23] A. Albarbar et al. „Performance evaluation of MEMS accelerometers“. *Measurement* 42.5 (2009), pp. 790–795. DOI: `10.1016/j.measurement.2008.12.002`.

[24] F. Mohd-Yasin, C. E. Korman, and D. J. Nagel. „Measurement of noise characteristics of MEMS accelerometers“. *Solid-State Electronics* 47.2 (2003), pp. 357–360. DOI: `10.1016/s0038-1101(02)00220-4`.

[25] Analog Devices. *Accelerometer Specifications - Quick Definitions.* May 18, 2017. URL: `http://www.analog.com/en/products/landing-pages/001/accelerometer-specifications-definitions.html`.

[26] Arduino.cc. *Arduino-introduction.* May 26, 2017. URL: `https://www.arduino.cc/en/guide/introduction`.

[27] Adafruit Industries. *Adafruit Website.* 2017. URL: `https://learn.adafruit.com/adafruit-ultimate-gps-logger-shield/overview`.

[28] F. Leens. „An introduction to I2C and SPI protocols“. *IEEE Instrumentation & Measurement Magazine* 12.1 (2009), pp. 8–13. DOI: `10.1109/mim.2009.4762946`.

[29] K. Urbanski and R. Woitowitz. *Digitaltechnik: Ein Lehr- und Übungsbuch.* 2013.

[30] S. van der Walt, S. C. Colbert, and G. Varoquaux. „The NumPy Array: A Structure for Efficient Numerical Computation“. *Computing in Science & Engineering* 13.2 (2011), pp. 22–30. DOI: `10.1109/mcse.2011.37`.

[31] E. Jones, T. Oliphant, P. Peterson, et al. *SciPy: Open source scientific tools for Python.* 2001. URL: `http://www.scipy.org/`.

[32] R. Boynton. „Precise Measurement of Mass“. *Sawe Paper No. 3147* (2001). URL: `https://www.space-electronics.com/contentAssets/Literature/Precise_Measurement_of_Mass.PDF`.

[33] H. Moritz. „Geodetic reference system 1980“. *Bulletin Géodésique* 54.3 (1980), pp. 395–405. DOI: `10.1007/bf02521480`.

[34] C. M. R. Fowler. *The Solid Earth: An Introduction to Global Geophysics*. Cambridge University Press, 2004. ISBN: 1139643320, 9781139643320.

[35] SensorsONE Ltd. *Local Gravity Calculator*. Nov. 15, 2017. URL: `https://www.sensorsone.com/local-gravity-calculator/#local-gravity`.

[36] I. Bronstein et al. *Taschenbuch der Mathematik*. 2008.

[37] T. J. Terrell. *Introduction to Digital Filters*. Palgrave Macmillan UK, 1988. DOI: `10.1007/978-1-349-19345-5`.

[38] K. C. Yeh and K. C. Kwan. „A comparison of numerical integrating algorithms by trapezoidal, Lagrange, and spline approximation“. *Journal of Pharmacokinetics and Biopharmaceutics* 6.1 (1978), pp. 79–98. DOI: `10.1007/bf01066064`.

[39] C. Mercer. „Acceleration, Velocity and Displacement Spectra – Omega Arithmetic“. *Prosig Signal Processing Tutorials* (2006). URL: `http://prosig.com/wp-content/uploads/pdf/blogArticles/OmegaArithmetic.pdf`.

[40] S. Han. „Measuring displacement signal with an accelerometer“. *Journal of Mechanical Science and Technology* 24.6 (2010), pp. 1329–1335. DOI: `10.1007/s12206-010-0336-1`.

[41] *Fritzing*. URL: `http://fritzing.org`.

Appendix

A. Wiring Diagram

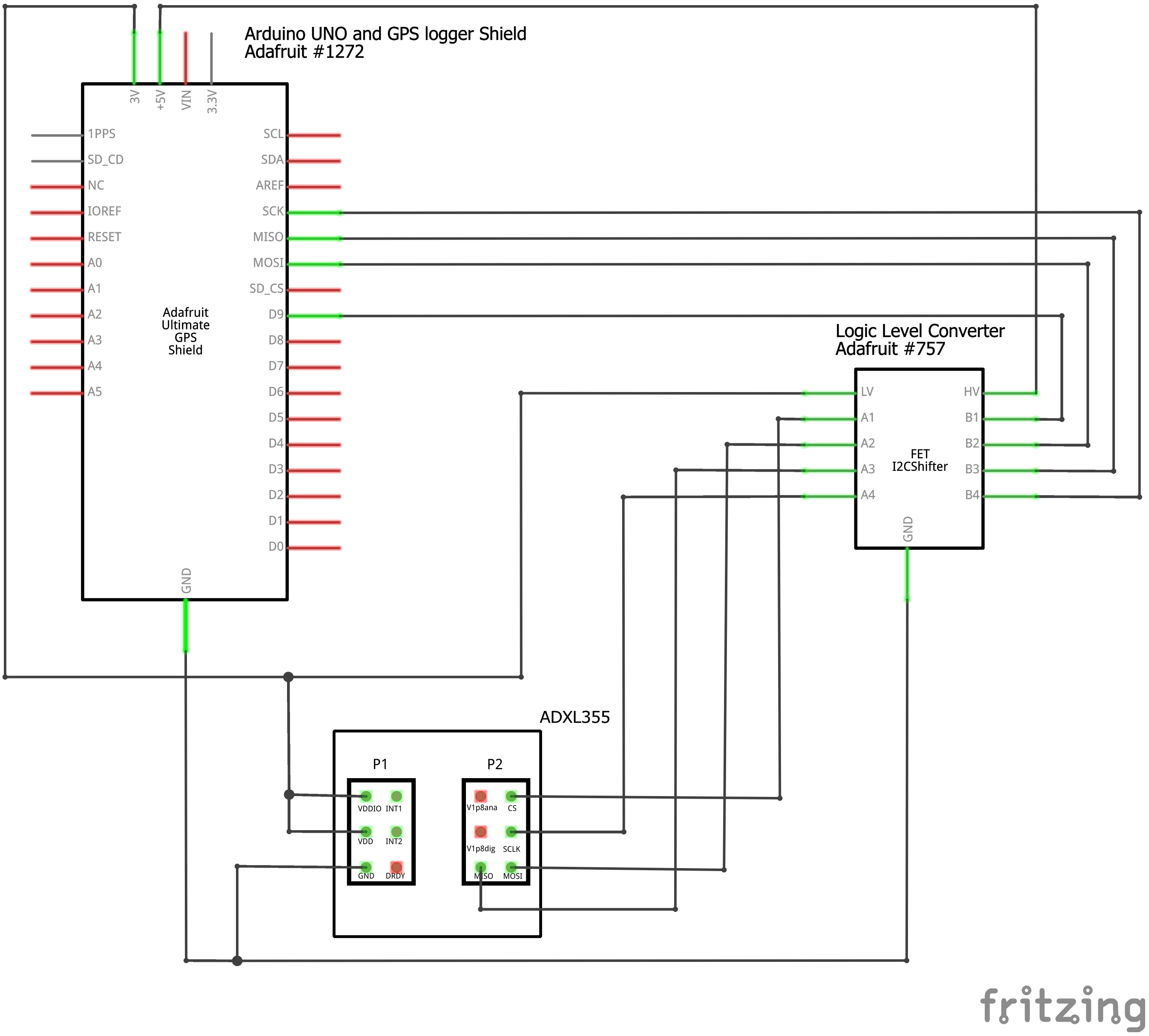

Figure 28: Wiring diagram of the sensor device. Pin names of the ADXL355 (left to right, top to bottom): P1: VDDIO, INT1, VDD, INT2, GND, DRDY; P2: V1p8ana, CS, V1p8dig, SCLK, MISO, MOSI. This image was created with Fritzing [41].

Acknowledgments

At this point, I would like to thank everyone that helped me during the creation of my master's thesis. Special thanks to:

- Prof. Dr. Christopher van Eldik for supervising my work and always providing valuable insight, explanations and feedback
- Prof. Dr. Stefan Funk for the second assessment
- Domenico Tiziani and Manuel Kraus for bringing the sensor to Namibia and conducting the measurement
- Maximilian Schandri, Christopher Sobel, Kristof Kremer and Christopher Schönwälder for providing a fun working environment in our office and for some good discussions
- Everyone involved in the H.E.S.S. and CTA groups for the friendly atmosphere and general helpfulness
- Leonie Bach and Karoline Herbst for proof-reading my work
- My family for being the greatest source of support and motivation one could hope for

Erklärung

Hiermit bestätige ich, dass ich diese Arbeit selbstständig und nur unter Verwendung der angegebenen Quellen und Hilfsmittel angefertigt habe.

Erlangen, den 16. Februar 2018

Christian Kupfer